# Geochemistry of the Gondwana sequence in the eastern Nepal Lesser Himalaya: Implications for provenance

**Drona Adhikari[1, 2] , Lalu Prasad Paudel[2], [3,4]Haritabh Rana, [3]Aman Soni[3] &**

**\*Harel Thomas[3]**

1.  Department of Geology, Tri-Chandra Multiple Campus, Tribhuvan University, Ghantaghar, Kathmandu, Nepal

2.  Central Department of Geology, Tribhuvan University, Kirtipur Kathmandu, Nepal

3.  Geological Survey of India, Dehradun Uttarakhand, India

4.  Department of Applied Geology, Dr. Harisingh Gour Vishwavidyalaya, (A Central University) Sagar (M.P.) India, 470004

Corresponding Author: Harel Thomas

## 1. Abstract:

The Barahakshetra–Ranitar area of eastern Nepal preserves a succession of Lower to Upper Gondwana sediments within the extra-peninsular Lesser Himalaya, yet detailed geochemical investigations of these sediments remain limited. The succession comprises the Permo-Carboniferous Kokaha Diamictite, the Permian Tamrang Formation with Baraha Volcanics, and the Late Cretaceous to Early Paleogene Sapt Koshi Formation. Provenance has been assessed through petrographic observations and whole-rock geochemical analyses (XRF and ICP-MS). Major oxide data show high $SiO_2$ contents (44.8–80.9 wt%) with variable $Fe_2O_3$ and $K_2O$, while weathering indices (CIA 64–77, PIA 82–93, CIW 82–99) indicate moderate to intense chemical

weathering in the source areas, except for one tuff sample from the Baraha Volcanics that records limited alteration. Trace element and REE signatures, including LREE enrichment, negative Eu anomalies, and elevated Zr/Sc and Th/Sc ratios, point to a felsic-dominated continental provenance. These characteristics are consistent with derivation from Archean to Proterozoic granitoid provinces of the northern Indian craton, particularly the Bundelkhand and Chotanagpur Granite–Gneiss complexes.

**Key Words:** Gondwana sequence; Barahakshetra–Ranitar; provenance; geochemistry; Indian craton

## 2. Introduction

During the Neoproterozoic era, large continental landmasses including present-day South America, Africa, Antarctica, Australia, the Indian subcontinent, and the Arabian Peninsula assembled in the southern hemisphere of the globe, forming the supercontinent Gondwanaland (Audley-Charles, 1983; Storetvedt, 1990; Valdiya, 1995; Van der Voo et al., 1999; Golonka and Bocharova, 2000; Veevers, 2004). The supercontinent began to break apart during the Early Jurassic period. The geological time sequence during which Gondwanaland remained welded is referred to as the Gondwana time period (Khadka et al., 2025). This interval is broadly classified into two subdivisions: the Lower Gondwana, which represents sedimentary sequences and geological events up to the end of the Permian period, and the Upper Gondwana, which refers to deposits and processes of the Mesozoic era (Sakai, 1983; Khadka et al., 2025).

During the Gondwana time, the supercontinent experienced several phases of rifting, extension, and subsidence, which led to the formation of sedimentary basins. Geomorphologically, these are referred to as rift valleys and half-grabens. In the case of the present-day Indian subcontinent, these sedimentary rock sequences are distributed both within the continental interior, known as

the Peninsular Gondwana sequences (Venkatachala and Tiwari, 1987; Valdiya, 1997; Dutta, 2002; Tewari and Maejima, 2010), and as several deformed patches within the Lesser Himalayan belt, known as the extra-peninsular Gondwana sequences (Acharyya, 1978; Kapoor and Singh, 1987; Tripathi and Singh, 1987; Sakai, 1983; Dhital, 1992; 2015;).

The peninsular basin sequences are distributed across various regions of Indian craton and are named as follows: the Damodar Basin (Casshyap and Kumar, 1987; Gupta, 1999), Son–Mahanadi Basin (Chowdari et al., 2022; Acharyya, 2019), Godavari Basin (Dasgupta et al., 2022; Rao, 1993), Wardha–Pranhita Basin (Nahak et al., 2025; Saha and Chaudhari, 2003), and Satpura Basin (Ghosh and Sarkar, 2010; Mall and Sharma, 2009). The sedimentary sequences in these basins predominantly exhibit fluvial and lacustrine depositional environments (Chakraborty and Sarkar, 2005; Dutta, 2002; Mishra et al., 2004; Maejima et al., 2004; Dasgupta, 2021), with sediments sourced from the surrounding Precambrian crystalline basement rocks, including the Archean Granite–Gneiss Complexes, Proterozoic sedimentary and metamorphic belts, Dharwar Craton rocks, Eastern Ghat Mobile Belt, and the Bastar, Singhbhum, and Chotanagpur Cratons.

The extrapeninsular sequences are located within the active mobile belts of the Himalaya, where they are often disrupted and weakly metamorphosed (Sakai, 1983). The sediments in these regions were deposited in rift valleys as well as in the passive continental margins and record a range of depositional environments, including glacial, glaciomarine, glaciofluvial, fluvial-deltaic, and purely fluvial settings (Bashyal, 1980, Sakai, 1983; Dhital, 1992; DeCelles et al., 2004; Najman et al., 2005). The Permo-Carboniferous deposits of Arunachal Pradesh have been interpreted as products of craton-interior and recycled-platform sources, accumulated within rift and collisional tectonic settings (Gogoi et al., 2025). In the Darjeeling area, within the Ranjit

Window, the Ranjit Pebble Slate Formation of comparable age has been studied through whole-rock geochemistry of shale and sandstone, revealing deposition in glaciomarine to fluvio-deltaic environments within a passive continental margin, derived from felsic-rich continental sources as well as the Peninsular cratons (Priya et al., 2021).

In the Nepal Himalaya, extra peninsular Gondwana sequences occur as isolated lithological pockets within the Lesser Himalayan domain, including Jajarkot–Piuthan–Salyan (Sharma et al., 1984), Dang (Dhital & Kizaki, 1987), Surkhet (Shrestha et al., 1987), Tansen (Sakai, 1983; Neupane et al., 2018), Katari (Dhital, 2015), Barahakshetra (Auden, 1935; Bashyal, 1980; Dhital, 1992; Sitaula, 2009; Dhital, 2015; Bhandari et al., 2019; Baral et al., 2022; Adhikari et al., 2023a, b), Dharan (Rai et al., 2016; Adhikari et al., 2020), and the Kankai section (Sharma, 1990). The Gondwana sequences of western Nepal have been studied more extensively than those of other regions. Sakai (1983) described the lithology, structure, and fossil assemblages of the western Nepal sequences, noting that the Permo-Carboniferous tillitic unit reflects glacial and glaciofluvial deposition with sediments derived from the Malani Granite and Vindhyan System. Overlying rhythmite beds of similar age were deposited in a shallow-marine setting. The Upper Gondwana Taltung Formation represents fluvial deposition with strong affinity to the Peninsular Shield, whereas the younger Amile Formation, deposited during the closing stages of Gondwana, is predominantly non-marine with locally fossiliferous shallow-marine horizons. The petrographic, heavy mineral, geochemical, mineral chemical, and detrital muscovite dating studies by Sitaula (2009) on sandstones from both western Nepal (Tansen Group) and eastern Nepal (Katari Group and Barahakshetra Group) suggest that most Gondwana sequences developed in continental settings along a passive margin, with occasional marine incursions. These records also indicate at least one episode of rifting during the Gondwana period. The

Permo-Carboniferous Tansen Group was sourced from igneous and metamorphic suites of the Malani Granite, Vindhyan Group, and Chotanagpur Gneissic Terrain, with deposition dominated by glacial and glaciofluvial processes. The Upper Gondwana Taltung and Amile formations share similar provenance with the Permo-Carboniferous unit. Post-Gondwana formations, such as the Bhainskati and Dumri, received detritus from both the Himalayan orogenic belt and the Indian Craton, with the Dumri representing foreland basin sedimentation.

Geochemical studies of the Upper Gondwana Amile and Post-Gondwana Bhainskati Formation from the Tansen area (Neupane et al., 2018) indicate that the Amile Formation was sourced from the northern Archean block or early–late Paleozoic lower Lesser Himalayan units. Khadka et al. (2025) further noted that the Lower Gondwana deposits in the Tansen area formed through glacial meltwater and fluvial sedimentation in a continental rift valley, whereas the Upper Gondwana units accumulated in swampy, deltaic, or low-energy floodplain environments under humid conditions along a passive continental margin. Provenance signatures suggest that both Lower and Upper Gondwana deposits were derived either from the Greater Himalaya (or Tethys Himalaya) or from sources sharing Indian-affinity detritus, whereas Post-Gondwana units dominantly record a Himalayan provenance.

In eastern Nepal, the Barahakshetra–Ranitar section hosts Gondwana rock sequences within the metasedimentary units of the frontal part of the Lesser Himalaya. The presence of these sequences was first recognized by Auden (1935), and later mapped and stratigraphically documented by Bashyal (1980), Dhital (1992; 2015), and Adhikari et al. (2023a, b). Bashyal (1980) also conducted whole-rock geochemical analysis, identifying granitic and metamorphic source rocks and suggesting deposition in epicontinental paralic basins with open marine connections during the early stages, transitioning to purely continental conditions in later phases.

Sitaula (2009) proposed that Gondwana sequences throughout the Nepal Himalaya were derived from igneous and metamorphic terrains of the Indian continental block. In contrast, Bhandari et al. (2018) argued that the Gondwana sequences were derived either from the Greater Himalaya (or the Tethys Himalaya) or from source regions sharing provenance with the Greater Himalaya. Baral et al. (2022) suggested that Lower Gondwana sediments were sourced from the Tethys Himalaya, while Upper Gondwana deposits incorporated detritus from the Lhasa Terrane, South Qiangtang Terrane, and Indo-China Block.

Recent works by Adhikari et al. (2025, in press) have presented a revised lithostratigraphy and age of the sediments based on detailed field mapping, petrographic study and newly discovered fossil records. In this context, it is appropriate to interpret provenance of the sediments using petrographic and geochemical data.  For this purpose, systematic samples were collected representing all the stratigraphic units and were observed under petrological microscope at the Central Department of Geology, Tribhuvan University and geochemical analysis was carried out at the Wadia Institute of Himalayan Geology (WIHG) in Dehradun. This paper presents the petrographic and geochemical data and their implications on the provenance analysis.

## 2. Geological Setting

### 2.1 Tectonic setting

The eastern Nepal Himalaya is morphotectonically divided into four distinct units, delineated by major east-west trending thrusts. From south to north, these units include: the Siwalik, composed of molasse-like sedimentary rocks; the Lesser Himalaya, characterized by sedimentary and metasedimentary sequences; the Higher Himalaya, consisting of high-grade metamorphic rocks; and the Tibetan Tethys Himalaya, which comprises sedimentary rocks overlying the elevated mountain peaks. These units are structurally separated by the Main Boundary Thrust (MBT), the

Main Central Thrust (MCT), and the South Tibetan Detachment System (STDS), successively

from south to north (Gansser, 1964; Frank & Fuchs, 1970; Upreti, 1999; Adhikari et al., 2021).

The Siwalik and the Lesser Himalaya exhibit limited surface exposure, while the Higher

Himalaya forms an extensive pseudosection due to its allochthonous, blanket-like cover over the

Lesser Himalaya, a result of thrusting along the MCT (Dhital, 2015; Ulak, 2016; Adhikari et al.,

2021) (Figure 1). The Lesser Himalaya is confined to a narrow belt parallel to MBT along the

Mahabharat Lekh, termed as the frontal Lesser Himalaya (Adhikari et al., 2023 a and b).

However, domal deformation and the deep gorges carved by the Arun and Tamor Rivers have

created tectonic windows, exposing the underlying Lesser Himalaya beneath the Higher
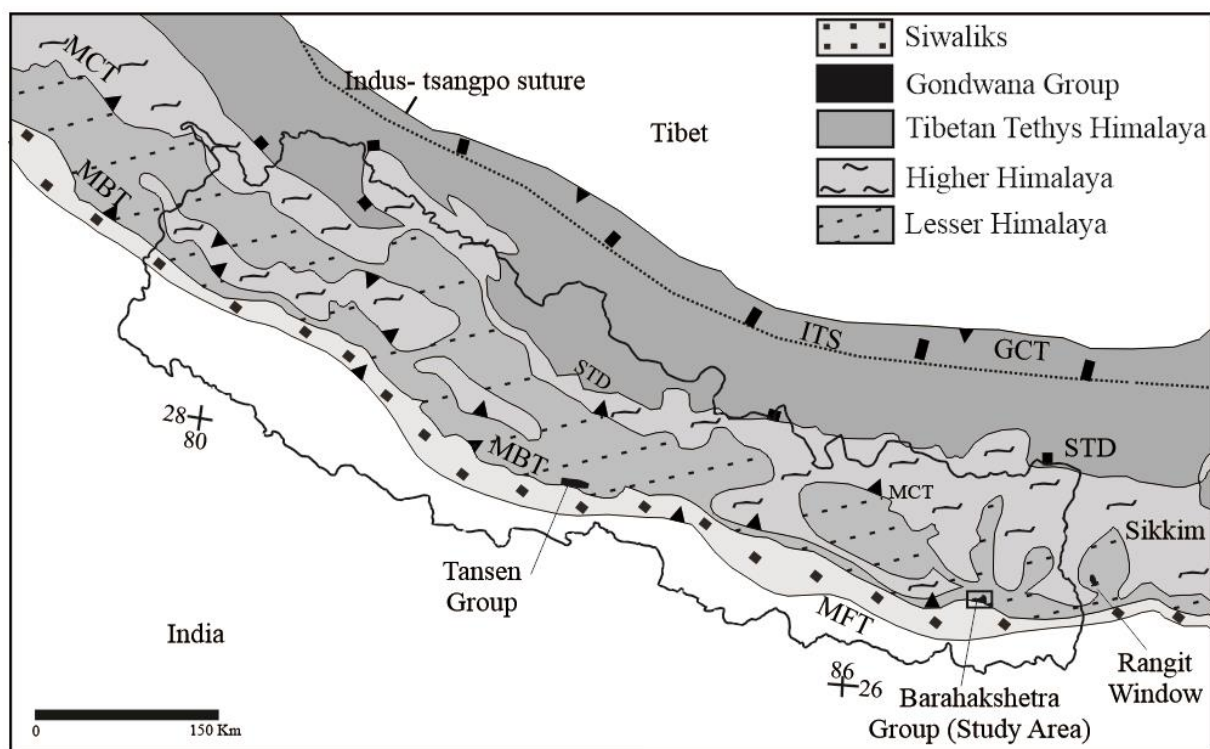
Himalayan rocks (Schelling, 1992).



**Figure 1**: Geological map of eastern flank of the central arc of the Himalaya with study area

marked as black box (detailed geological map at Figure 2a) (modified after  Robinson and

Pearson, 2013). MFT: Main Frontal Thrust, MBT: Main Boundary Thrust, MCT: Main Central

Thrust, STD: South Tibetan Detachment, GCT: Great Counter Thrust, ITS: Indus-Tsangpo

Suture.

## 2.2 Tectonolithostratigraphic division

The Barahakshetra-Ranitar area of eastern Nepal lies in the frontal Lesser Himalaya. The area is

tectonically divided into two Precambrian allochthonous sequences namely namely the Chimra

Thrust Sheet, the Dharapani Thrust Sheet and one paraautochthonous unit named as the Tribeni

Paraautochthon (Adhikari et al., 2023b). Both the allochthonous sequences are composed of

rocks of the Precambrian Lower Nawakot Group. The Tribeni Paraautochthon, which forms the

hanging wall of the MBT, consists of late Proterozoic stromatolitic dolomites of the Lukuwa

Dolomite unconformably overlain by the upper Carboniferous to early Tertiary Gondwana

sequence named as the Barahakshetra Group (Dhital, 1992; Adhikari et al. 2023b).

## 2.3. Lithostratigraphy of the Gondwana sequence

The Gondwana sequence in the Barahakshetra-Ranitar area is present as a narrow (~3 km N-W

width) linear belt (~13 km E-W extension) in the Lesser Himalaya (Figure 2a). The total

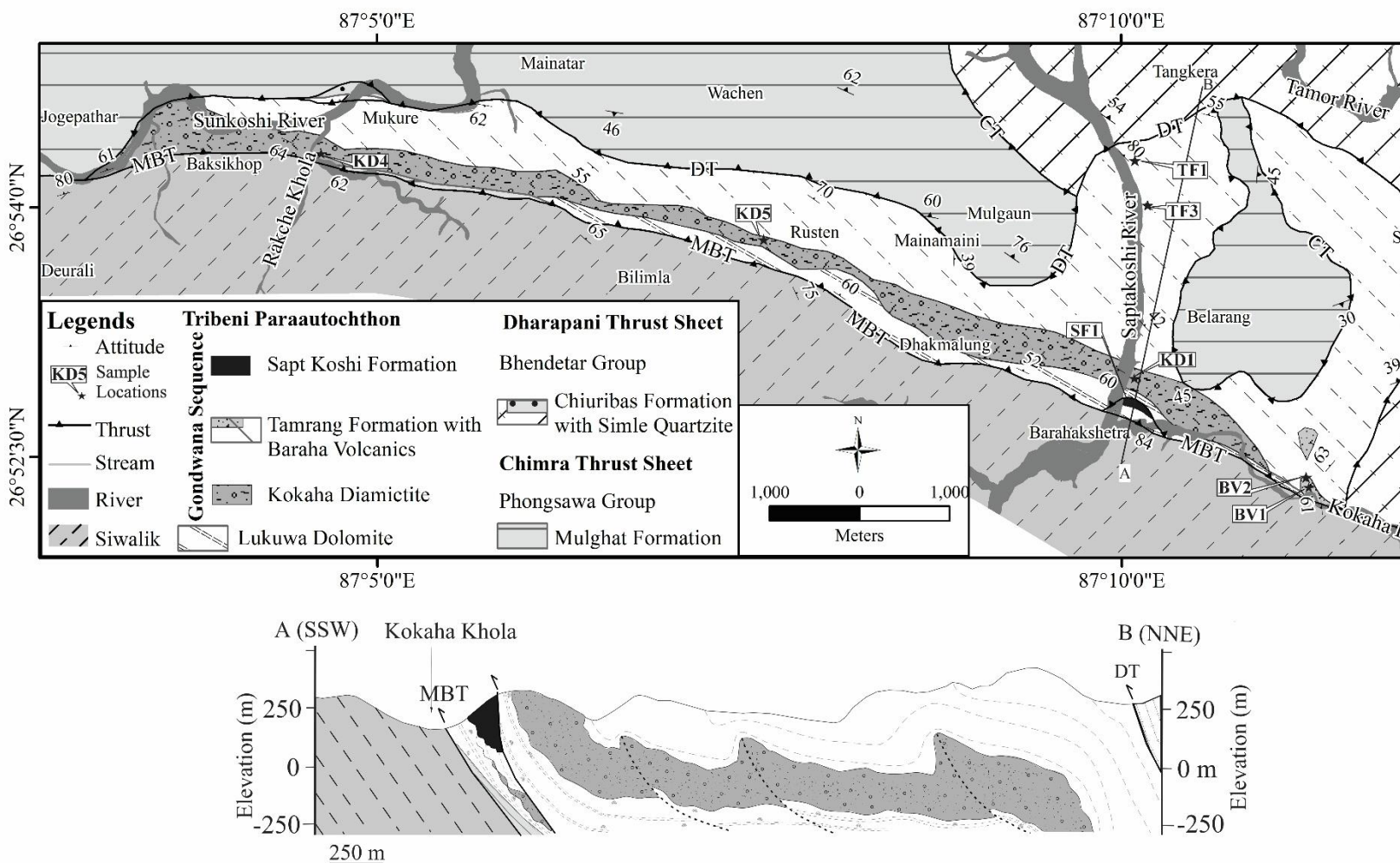stratigraphic thickness of the sequence reaches up to 800 m (Figure 3).

**Figure 2: (a)** Geological map of Barahakshetra – Ranitar area (regional location at Figure 1), eastern Nepal with locations of sample extracted. Sample numbers (eg.TF1) and their locations are shown on the map and also in the lithostratigraphic columns in Figure 3.  **(b)** Geological cross – section along line A -B of geological map in Figure 2a (Map and cross section modified from Adhikari et al. (2025, in Press). MBT-Main Boundary Thrust, DT- Dharapani Thrust, CT- Chimra Thrust.

**Figure 3:** Generalized stratigraphical section of Gondwana sequence of Barahakshetra – Ranitar area revised by Adhikari et al. (2025) (in press) with stratigraphic position of the sample extracted. Approximate stratigraphic horizon of the samples taken for petrographic and geochemical analysis are also shown in the figure.

The Gondwana sequence of the Barahakshetra – Ranitar area comprises of three lithological formations, namely Kokaha Diamictite, Tamrang Formation with Baraha Volcanics and the Sapt Koshi Formation in ascending order (Figures 2 and 3).

### 2.3.1 Kokaha Diamictite

The upper Carboniferous to lower Permian Kokaha Diamictite is characterized by conglomerate at the base containing clasts up to cobble size composed of pink to black chert and white quartzite embedded within a silica matrix, with clast sizes grading finer upward (Figure 3). This is overlain by a sequence of grey to black diamictite containing subangular clasts, up to boulder size, of grey, white, creamy, and green limestone and dolomite, as well as grey, pink, and white quartzite, red and black chert, black slate, granite, and gneisses. The diamictite is subsequently succeeded by a layer of fine-grained grey sandstone, grey siltstone, and grey to black shale that exhibits pencil cleavage. This sequence is overlain by diamictite sequences containing clasts similar to those found in the lower stratigraphic horizon. Overall, the formation has an average thickness of about 280 m.

### 2.3.2 Tamrang Formation with Baraha Volcanics

The lower to middle Permian Tamrang Formation exhibits an irregular contact with the Kokaha Diamictite and begins with a conglomerate of about 1.5 m thick (Figure 3). This conglomerate, which contains clasts similar as in the diamictite consists a medium-grained sand matrix marking the disconformable contact. The conglomerate is followed up-section by massive beds of bluish-grey, fine- to medium-grained calcareous sandstone with interbedding of thin to medium beds of grey marl and shale. At the Latare Khola section, the formation includes dark grey to dark green tuff and agglomerate composed of rounded sandstone and chert clasts within a tuff matrix, as well as dark grey to dark green volcanoclastic sandstone. This volcanoclastic unit, which is

observed within two stratigraphic horizons that pinch out in the western and eastern parts of the lower to middle section of the formation, is named as the Baraha Volcanics and is a member of the Tamrang Formation. The middle part of the formation is characterized by parallel-laminated sandstone and shale beds, while the upper section comprises of mollusca shell conglomerates, sandstone consisting cross-beds, climbing ripples, and current ripples, and shale beds. The average thickness of this formation is 450 m.

### 2.3.3 Sapt Koshi Formation

The upper Cretaceous to lower Tertiary Sapt Koshi Formation in the Barahakshetra-Ranitar area is present as a tectonic slice and is exposed only in Saptakoshi River section and Kokaha Khola section (Figure 2b). It unconformably overlies the Lukuwa Dolomite and is thrust over again in north by Lukuwa Dolomite.

The Sapt Koshi Formation consists of grey to dark grey carbonaceous quartzite, grey quartzite, grey to dark grey sandstone and shale (Figure 3). The sandstone and shale sequence comprises coal seams reaching up to 1 m in thickness. The average thickness of this formation is 75 m.

### 2.4 Petrography of samples

Eight rock samples were collected representing all lithologies and formations for the geochemical analysis. Among them, three samples (KD1, KD4 and KD5) belong to the Kokaha Diamictite, four samples (BV1, BV2, TF, TF3) belong to the Tamrang Formation with Baraha Volcanics, one sample (SF1) from the Sapt Koshi Formation (Figure 2a and 3). Petrographic description of each sample is given below.

### 2.4.1 Samples from the Kokaha Diamictite

### a. Diamictite (KD1)

Sample KD1 was collected from the left bank of the Saptakoshi River. It is composed of mud matrix (~74%) with quartz (~12%), feldspar (~4%), rock fragments (~5%), calcite (~4%), and minor other minerals (~1%). The rock fragments include chert and granites. The grains are predominantly angular (Figure 4a).

### b. Shale (KD4)

Sample KD4 was taken from the Rakche Khola section and consists of quartz (5%), calcite (3%), and fine silt and mud matrix (92%). Some quartz grains up to the size of fine sand are present. The mud and silt matrix shows development of bedding planes, and calcite veins cutting the bedding planes are common (Figure 4b).

### c. Sandstone (KD5)

Sample KD5 was obtained from the Mainamaini – Mulgau road section near Rusten Village and consists of quartz (65%), rock fragments (5%), matrix (5%), cement (20%), and others (5%) The grains are angular and poorly sorted with size ranging from 0.05 mm up to 1.3 mm. Most of the quartz grains are monocrystalline (65%). Zircon inclusions in quartz grain can also be observed. The cement is dark colored. Very few opaque minerals are present (Figure 4c).

### 2.4.2 Samples from the Tamrang Formation with Baraha Volcanics

### a. Sandstone (TF1)

Sample TF1 is a bluish grey calcareous sandstone obtained from the upper reaches of the Saptakoshi River and consists of quartz (~70%), rock fragments (~5%), muscovite (~5%), biotite (~5%), matrix (~10%), and cement (5%) The grains are angular to subangular and poorly sorted

with size ranging from 0.04 mm to 0.5 mm. The fractures in the grain are common. Both monocrystalline and polycrystalline quartz are present, and calcite serves as the cementing material. Mica grains aligned between quartz grains forming faint lamination (Figure 4d).

**b. Volcanoclastic sandstone (TF3 and BV2)**

Two samples of volcanoclastic sandstone were studied under the microscope. Sample TF3 was collected from the right bank of the Saptakoshi River and consists of a poorly sorted grains composed of volcanic lithic fragments (~ 55%), plagioclase feldspar (~25%), quartz (~10%), and fine-grained volcanic ash matrix (~10%) The volcanic lithic fragments, ranging from 0.2 to 0.8 mm, are sub-angular to angular and exhibit microlitic and lath-textured groundmasses. Plagioclase grains ranges in size from 0.1 to 0.6 mm, show polysynthetic twinning and moderate alteration to sericite. Quartz grains ranges from size 0.1 to 0.4 mm and display undulose extinction. The matrix is composed of altered volcanic ash with devitrified glass. Cementation is of calcite and silica (Figure 4e).

Sample BV1 is of volcanoclastic sandstone obtained from the right bank of the Latare Khola and consists of volcanic lithic fragments (~60%), plagioclase feldspar (~20%), quartz grains (~8%) and fine-grained matrix of devitrified glass (~12%). The lithic fragments are angular to sub-angular with size ranging from 0.15 to 0.75 mm in size and exhibits microlitic texture. Plagioclase feldspar with size range 0.1–0.5 mm shows moderate alteration to sericite. Quartz grains ranging from 0.1–0.3 mm, are sub-rounded. The sample is moderately to poorly sorted (Figure 4f).

**c. Tuff (BV2)**

Sample BV2 is greenish-grey tuff with abundant calcite veins, and was collected from the Latare Khola near its confluence with the Kokaha Khola. In thin section, it is composed predominantly of black, non-crystalline matrix resembling to volcanic glass (Figure 4g). Secondary calcite veins are prominent.

**2.4.3. Samples from the Sapt Koshi Formation**

**a. Sandstone (SF1)**

Sample SF1 is a black carbonaceous sandstone obtained from the left bank of the Sapt Koshi River about 300 m upstream from its confluence with Kokaha Khola and comprises quartz (~30%), rock fragments (~5%), matrix (~30%), cement (~25%), and minor components (~10%). The grains are angular to subrounded with size range from 0.04 to 0.7 mm. The rock fragments present include both volcanic and sedimentary fragments, mainly chert. The matrix appears to be formed by the alteration of larger grains into finer masses, and the cement is primarily black carbonaceous material. A few opaque minerals are present (Figure 4h).
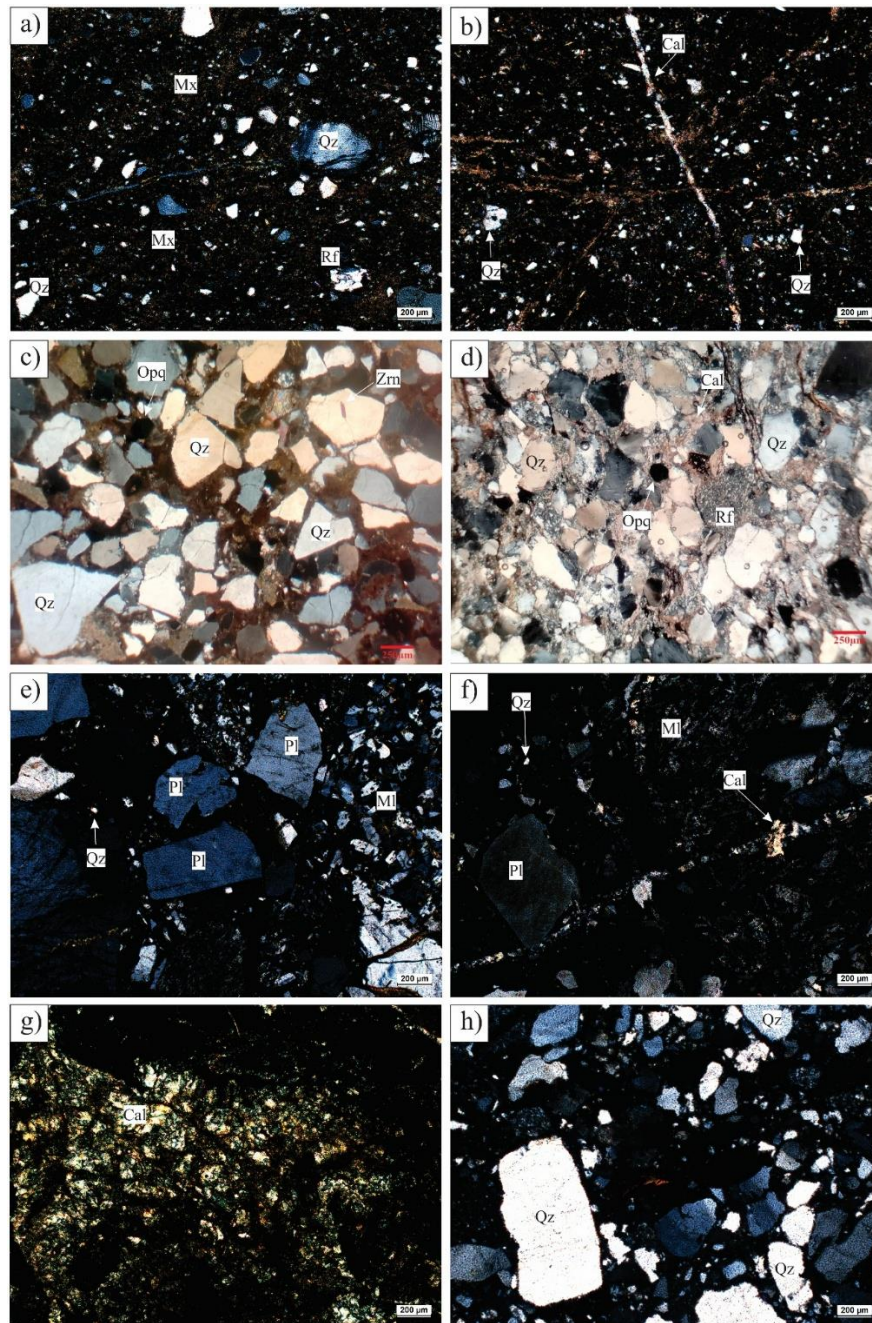
**Figure 4**: Photomicrographs of (a) KD1 showing poorly sorted, matrix dominated diamictite. The proportion of monocrystalline quartz is higher than polycrystalline quartz. (b) KD4 showing fine angular clasts of quartz embedded within mud along with calcite veins. (c) KD5 with dominant angular quartz grains. (d) TF1 showing poorly developed beddings indicated by orientation of mica between the quartz grains. (e) TF3 consisting microlites, plagioclase feldspar

and quartz clast within the glassy matrix. (f) BV1 showing larger grains of volcanic rock fragments with calcite cementing. (g) BV2 exhibiting calcite in dark glassy matrix. (h) SF1 showing poorly sorted sandstone with carbonaceous cement. Cal: calcite, Kfs: alkali feldspar, Ml: microlites, Mx: matrix, Opq: opaque mineral, Pl: plagioclase, Qz: quartz, Rf: rock fragments, Zn: Zircon.

## 3. Geochemistry

### 3.1 Instrument Specification and Sample Preparation Methodology

Whole-rock major oxides and trace element concentrations were assessed using pressed pellets on a wavelength dispersive X-Ray Fluorescence (WD-XRF) system, specifically the Bruker S8 Tiger, at the Wadia Institute of Himalayan Geology (WIHG) in Dehradun. The analytical precision of the XRF technique for both major and trace elements is reported to be within $\pm2$–3% and $\pm5$–6%, respectively. The rare earth elements (REEs) present in the representative volcanic rocks were analyzed using Inductively Coupled Plasma Mass Spectrometry (ICP-MS, ELAN DRC-E, Perkin Elmer), adhering strictly to the open digestion method at WIHG, Dehradun. Approximately 100 mg of the powdered sample was weighed using an electronic balance and treated with a mixture of 10 ml of distilled acids (HF: $HNO_3$) in a 1:2 ratio. The Teflon crucibles containing the acid-treated samples were placed on a hot plate, heated to approximately 200°C for several hours. Subsequently, about 2 ml of perchloric acid ($HClO_4$) was added, and the mixture was allowed to evaporate until dry. Once the samples had transformed into a thick brown paste, 10 ml of 1:1 $HNO_3$ was incorporated, and the samples were maintained on the hot plate for an additional 10 minutes. The final solution was then diluted to 100 ml in a volumetric flask, rendering it ready for REE analysis.

### 3.2 Geochemical Indices

The indices of chemical weathering consist of several essential metrics, including the Chemical Index of Alteration (CIA), the Chemical Index of Weathering (CIW), the Plagioclase Index of Alteration (PIA), and the Index of Compositional Variability (ICV). Eu/Eu∗ was computed as $(Eu)_{cn}/[(Sm)_{cn} \times (Gd)_{cn}] \times 0.5$ (McLennan, 1989), and Ce/Ce∗ was derived from $(Ce_{cn})/[(La_{cn} + Pr_{cn})] \times 0.5$. Here, cn signifies the chondrite-normalised values of the element (Taylor and McLennan, 1985). These indices play a vital role in determining the level of chemical weathering and the transformation of mineral compositions in geological studies (Table 1). In this investigation, all weathering indices, including CIA, PIA and CIW were applied due to their relevance in analyzing palaeo-weathering within the source area and explaining the compositional changes of the studied sandstones. Specifically, CIA, PIA, and CIW values of 60, 60–80, and more than 80 denote low to moderate and significant weathering intensities, respectively (Nesbitt and Young, 1982; Fedo et al., 1995; Harnois (1988)).

### 3.3 Major Oxides

The analysis conducted on a total of eight samples, which include three samples each of volcanoclastic sandstone (VSST) and sandstone (SST) along with a single sample each of

Table 1: Proxy and their formulaes used for the study

| Proxy Used | Formulae | Proposed after |
|---|---|---|
| CIA | $Al_2O_3/(Al_2O_3 + CaO* + Na_2O + K_2O)*100$ | Nesbitt and Young (1982) |
| PIA | $Al_2O_3\text{-}K_2O)/(Al_2O_3 + CaO* + Na_2O - K_2O)*100$ | Fedo et al. (1995) |
| CIW | $Al_2O_3/(Al_2O_3 + Ca_2O* + Na_2O)*100$ | Harnois (1988) |
|  |  |  |

diamictite and shale for major oxides, trace elements, and Rare Earth Elements (REE). Table 2a provides the results concerning the major oxides present in the eight samples. $SiO_2$ shows a range of 44.84% to 80.91% averaging at 67.06% while $Al_2O_3$ ranges from 6.91 % to 16.16 % averaging at 11.88%. Other major oxides values ranges as $Fe_2O_3$ (0.44% to 12.34%, avg. 5.59%), FeO (0.39% to 10.98%, avg. 4.97%), CaO (0.06% to 6.61%, avg. 1.38%), MgO (0.45% to 12.37%, avg. 2.81%), $Na_2O$ (0.03% to 1.95%, avg. 0.95%), $K_2O$ (1.51% to 4.82%, avg. 3.68%), MnO (0.00% to 0.12%, avg. 0.065%), and $TiO_2$ (0.43% to 6.39%, avg. 2.03). The classification shown in the diagram (Herron, 1988), Figure 5a, serves to differentiate various types of sediments according to their chemical composition. The X-axis $(log(SiO_2/Al_2O_3))$ represents quartz content and sediment maturity, while the Y-axis $(log(Fe_2O_3/K_2O))$ reflects the content of Fe-rich clay or heavy minerals in comparison to K-bearing minerals. The VSST plot is located within the "Shale" and "Wacke" zones, which indicates characteristics of immaturity, a matrix-rich texture, and the presence of lithic volcanic input. The sandstones vary from Fe Sand to Sub-arenite and Arkose, indicating differing levels of maturity, some are more feldspathic and quartz-rich, whereas others are rich in iron. Shale and diamictite are closely plotted within the "Shale" and "Wacke" zones, aligning with the properties of fine-grained and compositionally immature

sedimentary rocks. This plot verifies the prevalence of immature sediments (wackes or shales),

incorporating volcanoclastic elements and exhibiting varying degrees of compositional maturity

among the sandstones. The plot shown in Figure 5b proposed by Wronkiewicz & Condie, 1987 is

typically utilized for the classification of clastic sedimentary rocks according to geochemical

parameters. The X-axis ($K_2O/Na_2O$) indicates the feldspar composition where higher values

Table 2a: Major oxides analysis of the samples from Barahakshetra–Ranitar area of eastern

Nepal

| Sample | Name | BV1 | BV2 | TF3 | KD1 | KD4 | KD5 | SF1 | TF1 |
|---|---|---|---|---|---|---|---|---|---|
| | | Volcanoclastic Sandstone | Volcanoclastic Sandstone | Volcanoclastic Sandstone | Daimictite | Shale | Sandstone | Sandstone | Sandstone |
| $Na_2O$ | % | 1.00 | 1.42 | 1.22 | 1.95 | 1.57 | 0.03 | 0.04 | 0.33 |
| MgO | % | 0.45 | 12.37 | 1.71 | 2.39 | 3.49 | 0.84 | 0.15 | 1.04 |
| $Al_2O_3$ | % | 16.16 | 7.94 | 15.32 | 13.94 | 13.83 | 6.91 | 11.59 | 9.32 |
| $SiO_2$ | % | 63.08 | 44.87 | 63.11 | 64.97 | 64.13 | 76.49 | 80.91 | 78.95 |
| $P_2O_5$ | % | 0.14 | *1.27* | 0.12 | 0.15 | 0.10 | 0.31 | 0.02 | 0.13 |
| $K_2O$ | % | **10.41** | 3.44 | **9.37** | 3.64 | 3.57 | 1.17 | 0.08 | 2.14 |
| CaO | % | 0.29 | 6.61 | 0.63 | 1.05 | 0.80 | 0.28 | 0.06 | 1.35 |
| $TiO_2$ | % | *1.29* | **6.39** | 1.13 | 0.62 | 0.65 | *4.38* | 1.32 | 0.43 |
| MnO | % | 0.03 | 0.12 | 0.03 | 0.09 | 0.12 | 0.04 | 0.00 | 0.05 |
| $Fe_2O_3$ | % | 5.28 | 12.34 | 5.58 | 5.95 | 6.07 | 6.15 | 0.44 | 2.89 |
| SUM | % | 98.13 | 96.77 | 98.25 | 94.75 | 94.33 | 96.60 | 94.61 | 96.63 |
| L.O.I. | % | 1.35 | 6.49 | 2.01 | 3.84 | 4.21 | 2.59 | 5.10 | 2.70 |

Table 2b: Trace element analysis of the samples from Barahakshetra–Ranitar area of eastern

Nepal

| Sample | Name | BV1 | BV2 | TF3 | KD1 | KD4 | KD5 | SF1 | TF1 |
|---|---|---|---|---|---|---|---|---|---|
| | | Volcanoclastic Sandstone | Volcanoclastic Sandstone | Volcanoclastic Sandstone | Daimictite | Shale | Sandstone | Sandstone | Sandstone |
| Ba | PPM | *2092* | *2621* | *2015* | 716 | 585 | 549 | 155 | 378 |
| Cr | PPM | 32 | 630 | 19 | 74 | 75 | 307 | 100 | 82 |
| V | PPM | 58 | 378 | 59 | 106 | 125 | 310 | 97 | 54 |
| Sc | PPM | 4 | 21 | 3 | 8 | 8 | 10 | 9 | 4 |
| Co | PPM | 2 | 33 | 5 | 18 | 19 | 32 | 7 | 15 |
| Ni | PPM | 12 | 266 | 16 | 46 | 49 | 88 | 31 | 38 |
| Cu | PPM | 5 | 47 | 5 | 31 | 32 | 35 | 39 | 26 |
| Zn | PPM | 210 | 142 | 160 | 75 | 85 | 86 | 15 | 33 |
| Ga | PPM | *46* | 25 | *47* | 18 | 19 | 15 | 14 | 10 |
| Pb | PPM | 43 | 14 | 41 | 20 | 16 | 7 | 24 | 46 |
| Th | PPM | 29 | 9.9 | 28 | 26 | 30 | 14 | 18 | 14 |
| U | PPM | 5.2 | 2.3 | 6.6 | 1.9 | **BDL** | 1.7 | 2.6 | **BDL** |
| Sr | PPM | 644 | *9240* | 771 | 138 | 63 | 246 | 37 | 29 |
| Y | PPM | 44 | 41 | 40 | 28 | 25 | 21 | 25 | 19 |
| Zr | PPM | *1809* | *1009* | *1591* | 225 | 177 | 625 | *947* | 239 |
| Nb | PPM | 131 | 38 | 130 | 17 | 16 | 49 | 38 | 11 |

Table 2c: Rare earth element analysis of the samples from Barahakshetra–Ranitar area of eastern

Nepal

| Sample | BV2 | TF3 | KD1 | KD4 | SF1 | TF1 |
|---|---|---|---|---|---|---|
| | Volcanoclastic Sandstone | Volcanoclastic Sandstone | Daimictite | Shale | Sandstone | Sandstone |
| 139La | 162.072 | 423.906 | 61.128 | 49.02 | 10.482 | 43.164 |
| 140Ce | 400.524 | 867.21 | 99.012 | 116.886 | 15.87 | 86.904 |
| 141Pr | 59.004 | 112.638 | 14.67 | 11.982 | 2.73 | 9.852 |
| 142Nd | 234.69 | 394.062 | 51.06 | 42.138 | 9.138 | 36.414 |
| 152Sm | 37.668 | 56.532 | 9.552 | 7.944 | 1.494 | 7.092 |
| 153Eu | 9.894 | 11.82 | 1.746 | 1.296 | 0.288 | 1.284 |
| 156Gd | 24.756 | 38.064 | 8.394 | 6.672 | 1.248 | 6.15 |

| 159Tb | 2.958 | 4.65 | 1.29 | 1.02 | 0.21 | 0.93 |
|---|---|---|---|---|---|---|
| 164Dy | 13.158 | 21.606 | 7.386 | 5.934 | 1.29 | 5.136 |
| 165Ho | 1.836 | 3.288 | 1.338 | 1.038 | 0.252 | 0.9 |
| 166Er | 4.746 | 9 | 3.972 | 3.108 | 0.882 | 2.604 |
| 169Tm | 0.594 | 1.242 | 0.66 | 0.516 | 0.168 | 0.426 |
| 174Yb | 3.174 | 6.876 | 4.02 | 3.138 | 1.14 | 2.562 |
| 175Lu | 0.438 | 0.978 | 0.63 | 0.486 | 0.198 | 0.39 |

suggest an increased presence of K-feldspar (arkosic material), while lower values indicate a greater presence of Na-feldspar (plagioclase). The Y-axis ($SiO_2/Al_2O_3$) signifies maturity and quartz content where higher values reflect a greater quartz content and increased maturity. The VSST, shale, and diamictite situated within the greywacke and pelite greywacke regions exhibit intermediate to low $SiO_2/Al_2O_3$ ratios and moderate $K_2O/Na_2O$ ratios. This implies the existence of immature sediments that contain a significant matrix along with volcanic-lithic input. SST samples plotted in the fields of quartz-rich greywacke and quartz-rich arkose demonstrate high $SiO_2/Al_2O_3$ ratios and relatively moderate to high $K_2O/Na_2O$ ratios, indicating that these quartz-rich greywackes are likely derived from sources that have undergone extensive weathering or recycling. The plot of $K_2O/Al_2O_3$ versus $Na_2O/Al_2O_3$, shown in Figure 5c, provides a clear differentiation between sedimentary and igneous rocks, as described by Mackenzie and Garrels (1971). It is clear that all samples fall within the sedimentary rock field, with the exception of two SST samples and one VSST sample, which show lower $Al_2O_3$ levels in comparison to the other samples.

The CIA values for all samples are observed to range from 64.4 to 76.5, with the exception of one VSST sample that has a value of 34. These values are higher than those of PAAS (70) and UCC (52) (Nesbitt and Young, 1982). In a similar manner, the PIA values of the samples analyzed range from 82.2 to 93.2, with the exception of the same VSST sample, which has a

value of 27.98. The PIA values are higher than those of PAAS (79) and UCC (53) (Fedo et al.,

1995). Excluding the same VSST sample, which has a CIW below 80, the CIW for all other

samples is between 82 and 99, which is greater than those of PAAS (82) and UCC (58) (Harnois,

1988). According to the classification system proposed by Sprague et al. (2009), the chemical

classification of SST samples is categorized as sandstone to argillaceous sandstone, while VSST,

diamictite, and shale fall within the siltstone classification (Figure 5d), which is in agreement

with the petrological and other geochemical classifications, discussed in previous diagrams.
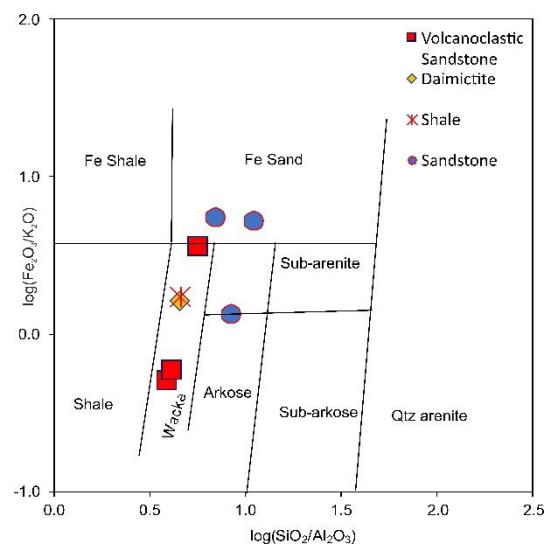


Figure 5a: log ($SiO_2/Al_2O_3$) versus log ($Fe_2O_3/K_2O$) (after Herron, 1988) for classification of

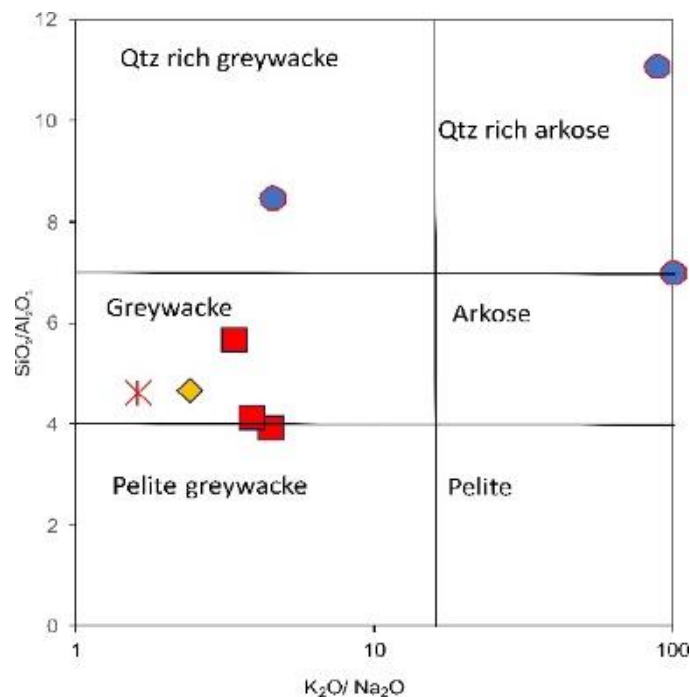terrigenous sediments and shales.

Figure 5b: $K_2O/Na_2O$ versus $SiO_2/Al_2O_3$ (after Wronkiewicz & Condie, 1987)
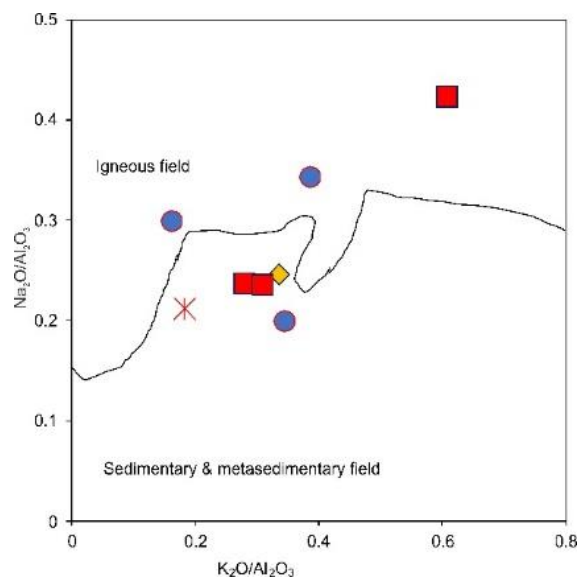


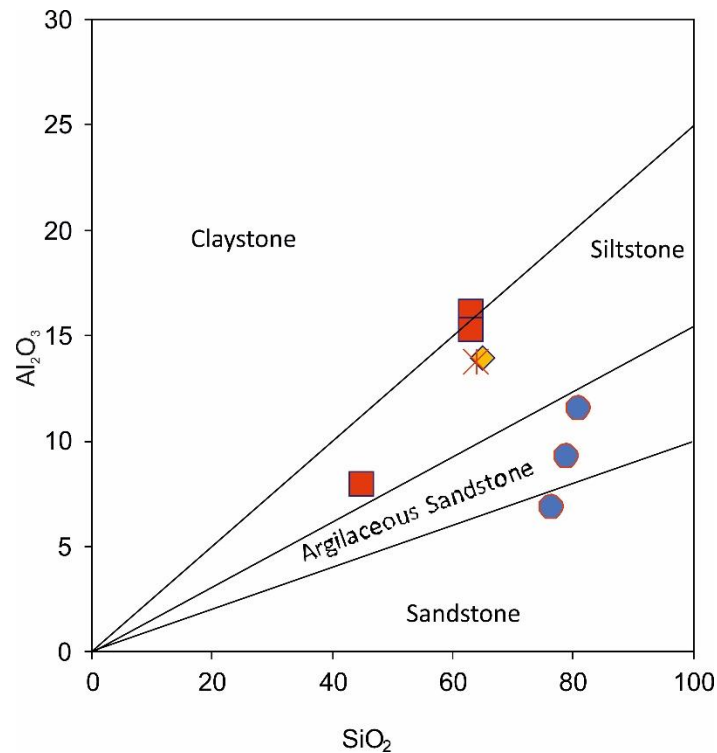Figure 5c: $K_2O/Al_2O_3$ versus $Na_2O/Al_2O_3$ (after Mackenzie and Garrels, 1971).

Figure 5d: Geochemical classification (after Sprague et al., 2009)

## 3.4 Trace Elements

Trace elements data of eight samples are shown in Table 2b. The trace elements data have been normalized with respect to the upper continental crust (UCC) and PAAS standard by Taylor and Mclennan (1985). The spider diagram of trace elements and rare earth elements after normalization have been plotted with respect to UCC and PAAS respectively shown in figure 6a and b, in which elements are arranged in order of decreasing compatibility. Most compatible elements are shown in the left followed by compatible elements towards the right on horizontal axis.

Ba (155- 2621 ppm, avg. 1137 ppm), exceed standard crustal values (Rudnick and Gao, 2003), indicating a notable enrichment in K-feldspar and mica-bearing source rocks. When normalized to the PAAS barium content of 668 ppm, the samples show enrichment factors from 0.23 to 3.92, with most samples reflecting moderate to high barium enrichment. The strong relationship between Ba and $K_2O$ content suggests that K-feldspar abundance is the primary controlling factor (Wilson, 1989; Rollinson, 1993). Cr (19 - 630 ppm, avg. 164 ppm) surpasses typical sedimentary rock values, indicating a considerable influx of heavy minerals from mafic sources (Rollinson, 1993). The chromium distribution pattern is bimodal, with most samples containing relatively low chromium values between 19 and 106 ppm, while sample BV2 shows high values. This pattern indicates a mixing of predominantly felsic sources with localized mafic-ultramafic inputs. Va (54 - 378 ppm, avg.148 ppm) indicates a strong correlation with the levels of iron oxide and titanium dioxide throughout the sample suite. The high Va concentrations, particularly in samples abundant in iron, suggest its incorporation into magnetite and ilmenite phases during the weathering and transport processes of source rocks (Canil, 1999). The Va/Cr ratio, which spans from 0.5 to 6.5, provides crucial constraints on the redox conditions of deposition and the characteristics of the source rock where elevated ratios indicate more reducing depositional environments and a significant contribution from intermediate to mafic igneous sources, while low ratios reflect more oxidizing conditions and a predominance of felsic sources. The concentrations of scandium are relatively low across the sample suite, ranging from 3 to 21 ppm, with an average of 9 ppm, indicating a minimal contribution from mafic sources. Upon normalization to the PAAS, scandium content of 16 ppm, most samples display depletion factors that range from 0.19 to 1.31, which confirms a predominant derivation from felsic source rocks. Cobalt (2 -33 ppm, avg. 14 ppm), displaying moderate enrichment in comparison to typical

crustal values. Ni (12 - 266 ppm, avg. 64 ppm), is showing a strong correlation with Cr and Co in analyzed samples (Sun & McDonough, 1989). Cu (5 - 47 ppm, avg. 23 ppm) is indicating moderate enrichment above typical crustal values, (Wedepohl, 1995) while Gallium (10 - 47 ppm, avg. 24 ppm), showing a strong correlation with $Al_2O_3$
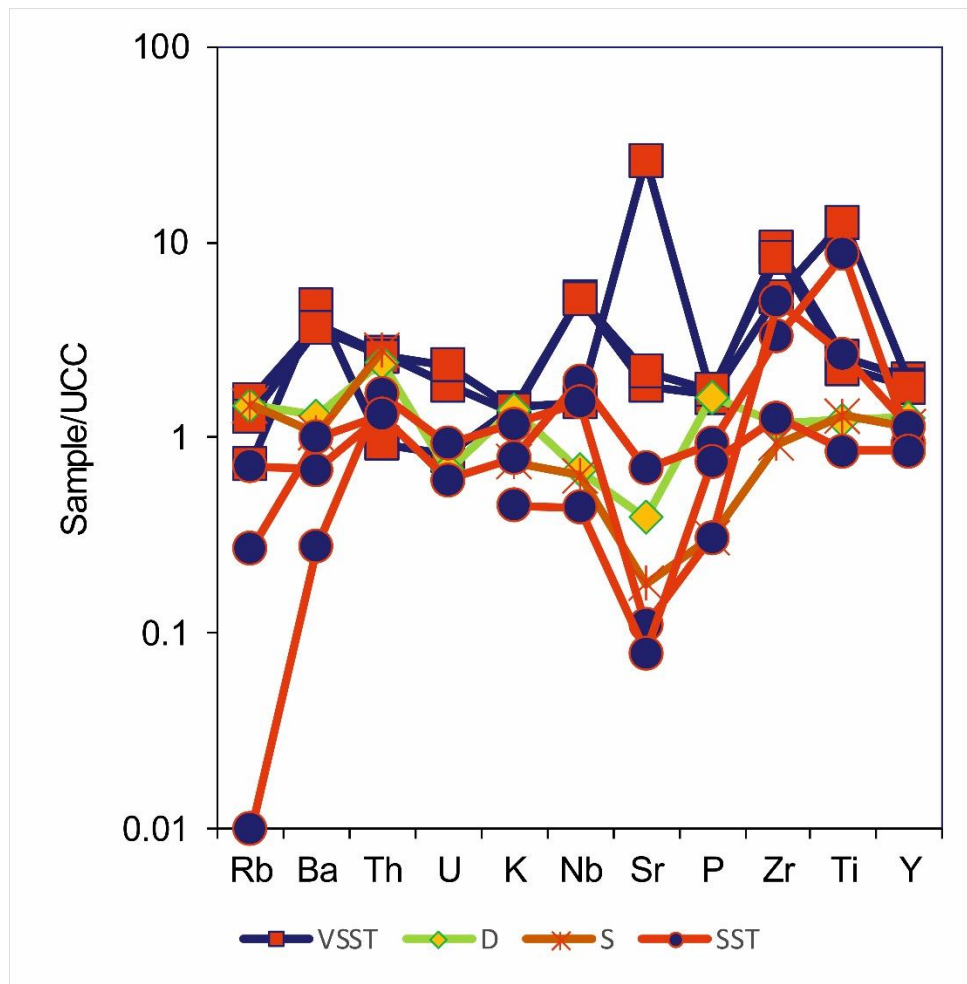


Figure 6a: Trace element variation diagram of all samples normalized to UCC (Taylor and McLennan, 1985)
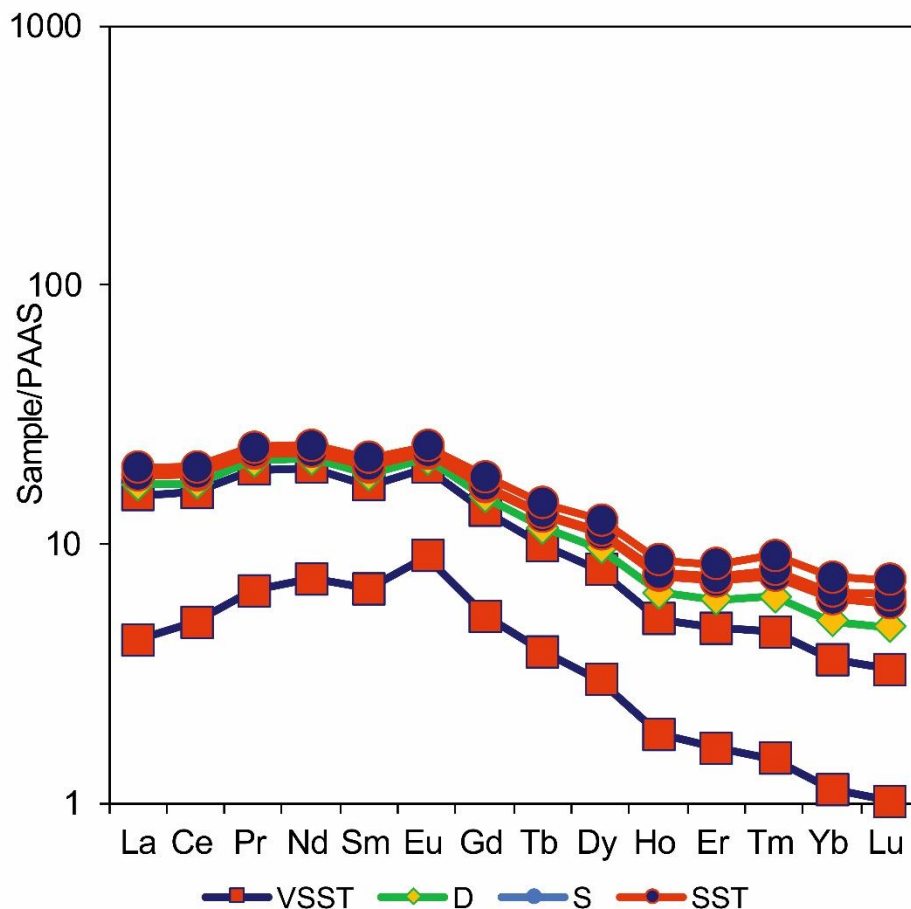
Figure 6b: Rare earth elements of all samples normalized to PAAS (Taylor and McLennan, 1985)

content throughout the sample suite. The distribution of gallium is primarily controlled by the abundance of feldspar and clay minerals, with the highest values occurring in samples with elevated aluminum content (Dostal & Capedri, 1978). The Ga/Al ratios range from 2.4 to 6.8, indicating typical crustal values and suggesting a derivation from evolved crustal sources signifying the occurrence of Al-rich minerals like feldspars and clay minerals. Pb (7-46 ppm, average 26 ppm) shows moderate values that are consistent with a crustal origin. The lead distribution is mainly influenced by K-feldspar and accessory mineral phases, with the highest concentrations found in samples that contain elevated potassium levels. Thorium (9.9 - 30 ppm,

avg. 22 ppm) showing moderate enrichment in comparison to PAAS values of 14.6 ppm. Rb (1-177 ppm, avg. 96 ppm) reveals a strong correlation with potassium oxide content throughout the sample suite. Strontium concentrations show wide range from 29 to 9240 ppm, with this exceptional range reflecting both primary source rock characteristics and secondary diagenetic processes. The high strontium concentration of 9240 ppm in sample KD4 is more than twelve times higher than the next highest concentration, suggesting significant diagenetic alteration involving carbonate precipitation or feldspar alteration (Rollinson, 1993). The remaining samples exhibit strontium concentrations between 29 and 771 ppm. Yttrium (19-44 ppm, avg. 30 ppm) is closely matching PAAS values of 27 ppm. The distribution of yttrium is predominantly influenced by heavy mineral phases, particularly zircon, xenotime, and heavy REE-bearing minerals. The moderate enrichment suggests a derivation from typical continental crustal sources (Bau, 1996). The Y/Ho ratio range from 26 to 44, which indicates standard crustal values and suggests limited fractionation during transport and deposition. Zirconium (177 - 1809 ppm, avg. 747 ppm), represents significant enrichment in comparison to PAAS values of 210 ppm. The distribution of zirconium is controlled by the abundance of zircon, with the highest concentrations found in samples with increased heavy mineral content. The Zr/Hf ratio range from 25 to 45, indicating typical crustal values and suggesting a derivation from evolved crustal sources. Zirconium enrichment is especially pronounced in volcanoclastic sandstones, where the average concentration is 1403 ppm, indicating a source from zircon-bearing felsic igneous rocks (Hoskin & Schaltegger, 2003). Niobium (11 - 131 ppm, avg. 46 ppm), indicates moderate to high enrichment compared to PAAS values of 19 ppm. The distribution of niobium is influenced by rutile, ilmenite, and other titanium-bearing minerals, with the highest concentrations found in samples that have increased titanium dioxide content (Pearce et al., 1984). The Nb/Ta ratios vary

from 12 to 18, reflecting typical crustal values and implying a source from evolved crustal materials.

## 3.5 Rare Earth Elements

REE data of eight analysed samples are tabulated in Table 2c. Lanthanum (10.48 - 423.91 ppm, avg. 140.8 ppm) is showing substantial enrichment relative to PAAS values of 38.2 ppm. The La/Yb ratios range from 1.06 to 61.58, indicating steep rare earth element slopes characteristic of continental crustal sources. Cerium (15.87 - 867.21 ppm, avg. 262.9 ppm) representing high enrichment relative to PAAS values of 79.6 ppm. The Ce/Y ratios range from 0.4 to 30.3, indicating strong light rare earth element (LREE) enrichment and suggesting derivation from felsic igneous sources. Praseodymium (2.73 - 112.64 ppm, avg. 35.1 ppm), shows substantial enrichment relative to PAAS values of 8.83 ppm. Neodymium (9.14 - 394.06 ppm, avg. 123.5 ppm) representing significant enrichment relative to PAAS values of 33.9 ppm. The Nd/Sm ratios range from 4.2 to 7.0, indicating typical crustal values and suggesting limited fractionation during transport and deposition. Samarium (1.49 - 56.53 ppm, avg. 18.6 ppm) showing substantial enrichment relative to PAAS values of 5.55 ppm. Europium concentrations span from 0.29 to 11.82 ppm, with an average of 4.17 ppm, representing significant enrichment relative to PAAS values of 1.08 ppm. The europium anomaly i.e. Eu/Eu*, ranges from 0.86 to 1.63, indicating slight positive europium anomalies in most samples. This positive europium anomaly is unusual for typical sedimentary rocks and suggests either plagioclase accumulation in the source region or reducing conditions during transport and deposition. Gadolinium concentrations range from 1.25 to 38.06 ppm, with an average of 12.2 ppm, showing substantial enrichment relative to PAAS values of 4.66 ppm. The gadolinium distribution marks the

transition from light to heavy rare earth elements (HREE), with its behaviour controlled by both monazite and xenotime mineral phases. Terbium (0.21 - 4.65 ppm, avg. 1.77 ppm), representing significant enrichment relative to PAAS values of 0.774 ppm.  Dysprosium (1.29 - 21.61 ppm, avg. 8.05 ppm), showing substantial enrichment relative to PAAS values of 4.68 ppm. The dysprosium distribution is controlled by xenotime and other heavy REE-bearing minerals, with moderate enrichment suggesting derivation from typical continental crustal sources. Holmium concentrations span from 0.25 to 3.29 ppm, with an average of 1.57 ppm, representing significant enrichment relative to PAAS values of 0.991 ppm. The Ho/Y ratios range from 0.023 to 0.037, indicating typical crustal values and suggesting limited fractionation during transport and deposition. Erbium (0.88 - 9.00 ppm, avg. 4.43 ppm), showing substantial enrichment relative to PAAS values of 2.85 ppm. Thulium (0.17 - 1.24 ppm, avg. 0.66 ppm), representing significant enrichment relative to PAAS values of 0.405 ppm. Ytterbium (1.14 - 6.88 ppm, avg. 3.55 ppm), showing moderate enrichment relative to PAAS values of 2.82 ppm. Lutetium (0.20 - 0.98 ppm, avg. 0.55 ppm), representing moderate enrichment relative to PAAS values of 0.433 ppm. The lutetium distribution closely follows that of ytterbium, thulium and erbium indicating control by similar heavy mineral phases such as xenotime, zircon and garnet.

## 4. Discussion

The analysis of major oxides, trace elements, and REE found in clastic sedimentary rocks provides crucial data for interpreting the provenance and paleoenvironmental conditions during the time of deposition. This technique has been broadly applied to infer the provenance of sedimentary formations (Moradi et al., 2016; Xie et al., 2018; Wei and Algeo, 2020; Xiao et al., 2023). The Gondwana sequence of eastern Nepal remains sparsely expored in terms of

geochemistry, with only limited whole rock geochemistry of Sapt Koshi Formation. The sandstones were Fe-rich indicating its derivation from the felsic source terrains along with high CIA values reflecting intense chemical weathering and REE showing recycled sedimentary or plutonic-metamorphic sources. In this investigation careful extraction of the samples covering the major lithologies of the Gondwana sequence were carried out following the revised lithologic distribution and stratigraphy including Permo-Carboniferous Kokaha Diamictite, Permian Tamrang Formation with Baraha Volcanics, and the Cretaceous to early Paleogene Sapt Koshi Formation. The compositions of major element oxides, trace elements, and rare earth elements were utilized to analyse paleo-weathering and provenance of the source rocks within the Gondwana basin of the Barahakshetra – Ranitar area.

## 4.1 Provenance from major elements

The elemental geochemistry, i.e. major, trace, and REE, of clastic sedimentary rocks has been used to infer their provenance (McLennan et al., 1993; Roser and Korsch, 1986; Augustsson et al., 2023). Certain oxides, such as $Al_2O_3$ and $TiO_2$, together with trace elements such as Sc, Ni, La, Co, Cr, V, Nb, Hf, Y, Zr and Th, show low mobility or immobility during the processes of transportation, weathering, and diagenesis of their parent rocks (Augustsson et al., 2023). The primary oxides are inadequate for precisely identifying the origin of siliciclastic rocks, as numerous oxides are prone to mobility due to weathering and diagenetic processes (Augustsson et al., 2023). Studies opined that the ratios of $K_2O/Na_2O$ and $Al_2O_3/TiO_2$ are reliable provenance indicators for terrestrial deposits (Hayashi et al., 1997; Roser and Korsch, 1986; Augustsson et al., 2023). Hayashi et al. (1997) claimed that Al and Ti are generally compatible and show immobility during both pre-depositional and post-depositional processes. Augustsson et al. (2023) illustrated that $K_2O/Na_2O$ ratios are effective for determining the source rocks of

sediments in arid climatic conditions and terrestrial depositional environments, unlike humid and marine settings. The ineffectiveness of $K_2O/Na_2O$ as a provenance indicator for sediments formed in terrestrial depositional environments with humid climates may be due to the significant weathering of $K_2O/Na_2O$ under such climatic conditions (Augustsson et al., 2023). According to Hayashi et al. (1997), the ratios of $Al_2O_3/TiO_2$ act as indicators of the type of source rock, with values ranging 3 to 8 suggesting mafic igneous origins, while ratios from 8 to 21 indicate intermediate igneous source rocks. In contrast, ratios that range from 21 to 70 are linked to felsic igneous source rocks. In the analysed samples, the $Al_2O_3/TiO_2$ ratio was found to range from 8.78 to 22.48 except for one sample falling at less than 2, These results are in close agreement with the characteristics of felsic and intermediate igneous sources (Figure 6c), as highlighted by Hayashi et al. (1997). In addition, plotting the bivariate diagram of $TiO_2$ versus Zr of Hayashi et al. (1997) documented the felsic and intermediate igneous provenance for the studied samples (Figure 6d).
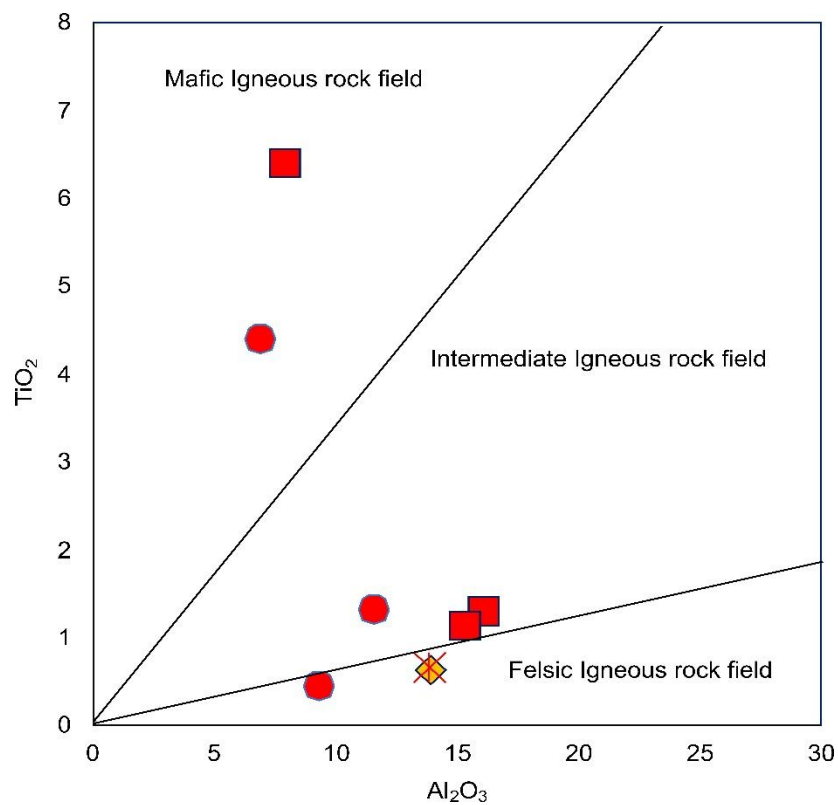
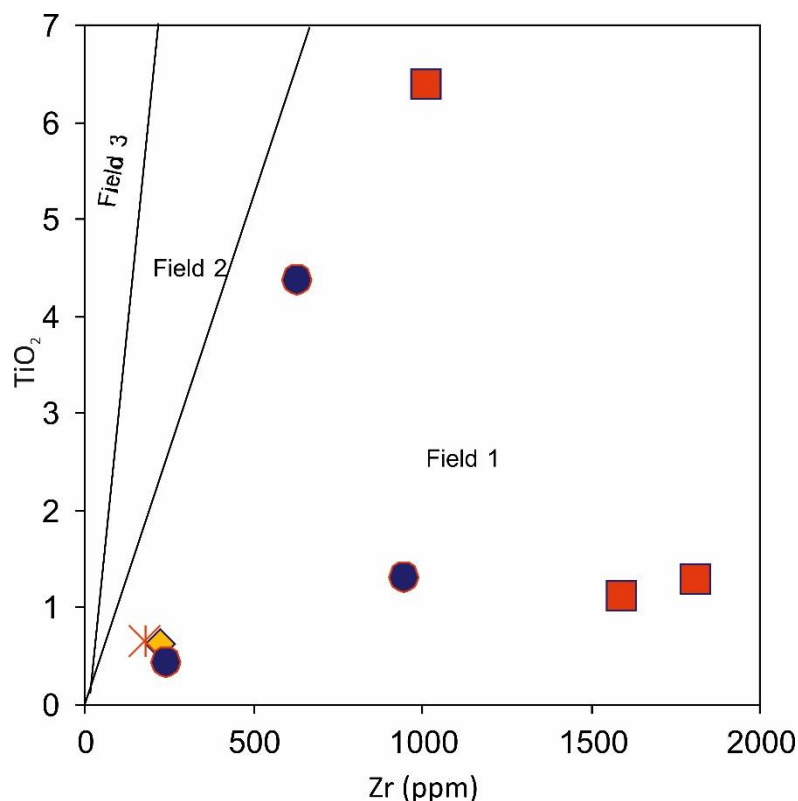Figure 6c: $Al_2O_3$ versus $TiO_2$ (after Hayashi et al., 1997),

Figure 6d: Zr (ppm) versusTiO$_2$ (wt%) (after Hayashi et al., 1997), field 1: felsic igneous rocks, field 2: intermediate igneous rocks, field 3: mafic igneous rocks

## 4.2 Provenance from trace elements

Trace elements such as Ti, Th, Sc, Nb, Y, Hf and Zr is imperative for determining the provenance of clastic sedimentary rocks. The stability and its compatible nature during recycling and diagenesis processes plays a major role as reliable indicators for deciphering the origins of these geological formations (Totten et al., 2000; Augustsson et al., 2023). The trace elements as discussed in section 3.3 shows that the Sr and P have high enrichment (*15-20 times) as compared to UCC, while Zr and Ti shows moderate enrichment. Rb, K and Nb shows depletion while Ba, Th and U remain close to UCC values with moderate variations. The trace elements values of analysed samples when plotted in bivariate diagrams such as Th/Sc versus Cr/Th

(Totten et al., 2000), (Figure 6e) and Y/Ni versus Cr/V (McLennan et al., 2003), (Figure 6f) shows the felsic affinity rather than the mafic ones.

The analysis reveals a notable contribution from a felsic igneous source, with only a slight input from a mafic igneous source in the examined samples. The low Cr/V ratios, relative to the Y/Ni ratios, point to a felsic origin for the sediments under investigation, effectively eliminating the chance of contributions from mafic or ultramafic sources (McLennan et al., 1993).
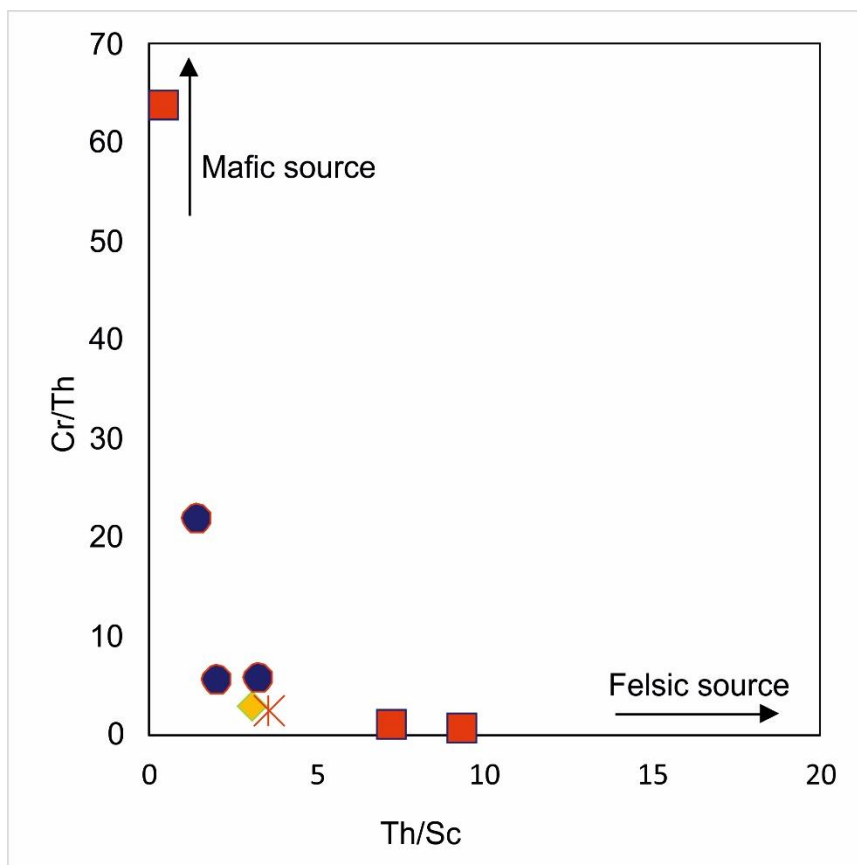


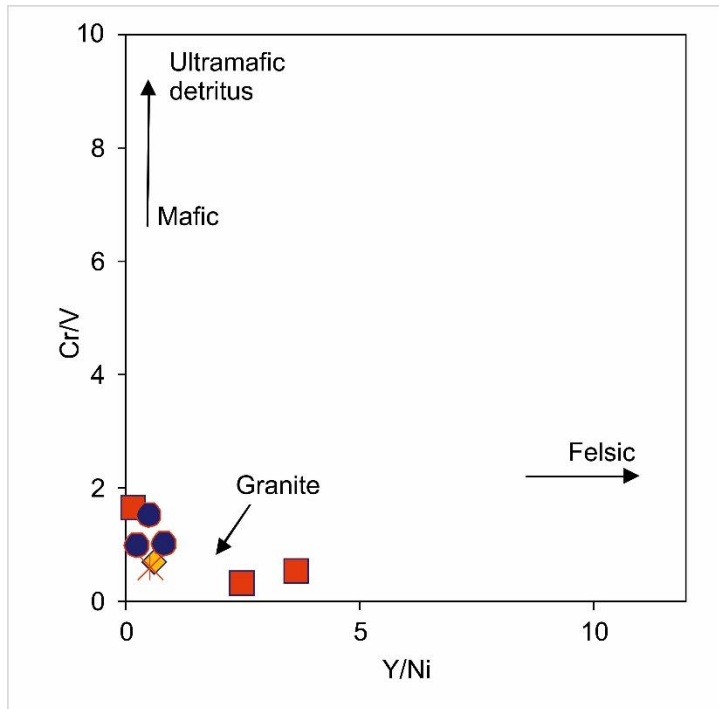Figure 6e: Th/Sc versus Cr/Th bivariate diagram

Figure 6f: Y/Ni versus Cr/V baivariate diagram

## 4.3 Provenance from REE

Owing to their constrained mobility and considerable stability throughout weathering,

transportation, and diagenetic processes of the parent rocks (Taylor and McLennan,

1985), REEs act as significant indicators for pinpointing the type of parent rocks from

which clastic rocks arise. The distribution pattern of REEs and europium anomalies in

clastic sediments offers substantial evidence for identifying the composition of source

rocks (Taylor and McLennan, 1985; Cullers, 1994; Rudnick and Gao, 2003; Armstrong-

Altrin et al., 2015). The high ratios of light rare earth elements (LREE) to heavy rare

earth elements (HREE) and the presence of negative europium (Eu) anomalies in clastic

rocks indicate a felsic source. In contrast, the lower LREE/HREE ratios and the absence

of Eu anomalies in clastic rocks point to a mafic source (Cullers, 1994). In the analysed

sample, the LREE averages 109.21 while the HREE averages 35.48 ppm while the

LREE/HREE ratio ranges from 7.83 to 23.67. The europium anomaly of the analysed

samples ranges from 0.21 to 0.936. The chondrite normalised values of (La/Yb)N ranges

3.02 to 31.78 averaging 17.33 while (Gd/Yb)N ranges from 1.39 to 3.13 averaging 2.28.

The elevated ration of LREE/HREE indicates a felsic igneous source (Cullers, 1994)

while the elevated average ratios of (La/Yb)N along with the lower side average ratio of

(Gd/Yb)N implies a granitic origin of the source rocks (Rudnick and Gao, 2003). The

elevated LREE/HREE ratios along with lower side of Eu anomalies reinforces the

conclusion that the Upper Continental Crust (UCC) has a granitic origin (Taylor and
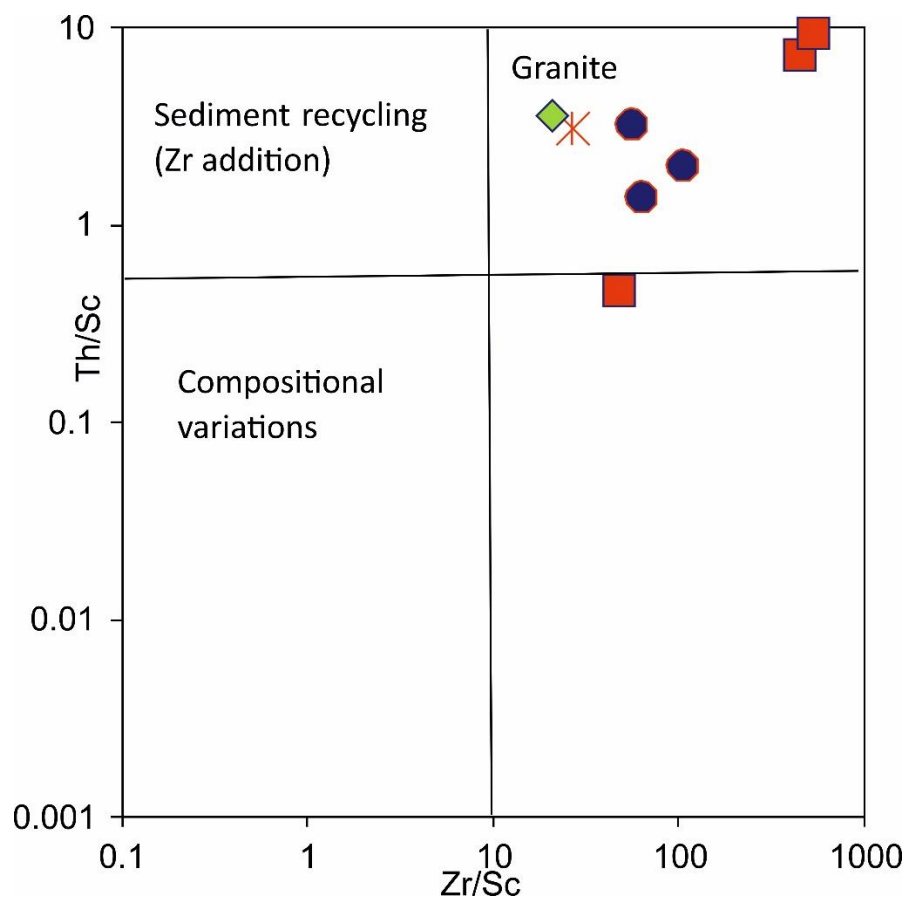
McLennan, 1985; Rudnick and Gao, 2003).



Figure 6g: Zr/Sc versus Th/Sc (after McLennan, 1993)

**Conclusion**

The petrographic and geochemical features of the Gondwana sediments in the Barahakshetra–Ranitar region indicate a significant provenance connection to the northern Indian cratonic terranes. The samples analyzed reveal elevated levels of $SiO_2$, $Al_2O_3$, $K_2O$, Th, Rb, and Zr, alongside enriched LREE and distinct negative Eu anomalies geochemical markers typically linked to felsic igneous rocks, especially granites and gneisses originating from the upper continental crust. These compositional characteristics align closely with the Archean to Proterozoic granitoid provinces of the Indian Peninsular Shield, particularly the Bundelkhand and Chotanagpur Granite-Gneiss Complexes, which are components of the northern Indian craton. During the Permo-Carboniferous period, the northern edge of the Indian plate experienced tectonic activity due to continental rifting related to the disintegration of Gondwanaland. This extensional environment revealed older cratonic rocks, facilitating their erosion and providing sediments to neighboring rift basins, including the Barahakshetra–Ranitar Gondwana basin. The high concentrations of Zr and Th, increased Zr/Sc and Th/Sc ratios, and the prevalence of monocrystalline quartz and K-feldspar noted in petrographic studies further corroborate a derivation from well-evolved, felsic plutonic sources. The lack of significant chemical weathering indicators in the source area, as suggested by moderate CIA values, is also in line with sediment supply from a relatively stable, semi-arid cratonic hinterland. Consequently, the compositional and tectonic framework reinforces a regional correlation between the Gondwana sedimentary deposits of eastern Nepal and the exposed granitoid and gneissic complexes of the Indian craton to the south. These cratonic highlands likely served as the main sediment sources for the Barahakshetra–Ranitar basin during Gondwanan times,

establishing a connection between the Lesser Himalayan foreland basins of eastern Nepal and the

intracratonic sediment dispersal systems functioning along the northern margin of Gondwana.

**References**

Acharyya, S. K. (1978). Stratigraphy and tectonic features of the eastern Himalaya. *Tectonic geology of the Himalaya*, 243-269.

Acharyya, S. K. (2019). Development of Gondwana basins in Indian shield. *In Developments in Structural Geology and tectonics*, 4, 17-29.

Adhikari, D., Niraula, K. P., Rai, P., Rijal, N., Agnihotri, D., & Paudel, L. P. (2025). Revised lithostratigraphy and age of the Gondwana Sequence in eastern nepal Himalaya. *Journal of Geological Society of India*, In Press.

Adhikari, D., Silwal, C. B., & Paudel, L. P. (2021). Review of the Geology of the Arun-Tamor Region, Eastern Nepal: Present Understandings, Controversies and Research Gaps. *Journal of Institute of Science and Technology*, 26(2), 79-97.

Adhikari, D., Silwal, C. B., and Giri, S. (2020). Geological and Geotechnical State of the Nisane Khola Landslide, Dharan, Sunsari, Nepal: a case study. *Himalayan Journal of Science and Technology*, 4, 24–31. https://doi.org/10.3126/hijost.v4i0.33862

Adhikari, D., Tamrakar, P., Khatiwada, P. P., Gyawali, R., & Paudel, L. P. (2023a). Quartz grain microstructures and microscopic shear sense indicators in the outer Lesser Himalaya, Barahakshetra-Tribeni-Raighat area of Arun Valley, eastern Nepal. *Journal of Nepal Geological Society*, 65(01), 175–182. https://doi.org/10.3126/jngs.v65i01.57776

Adhikari, D., Tamrakar, P., Khatiwada, P. P., Gyawali, R., & Paudel, L. P. (2023b). Tectono-lithostratigraphy of the outer Lesser Himalaya in the Barahakshetra-Tribeni area, Arun valley section, eastern Nepal. *Journal of Nepal Geological Society*, 66, 103-118.

Armstrong-Altrin, J. S., Machain-Castillo, M. L., Rosales-Hoz, L., Carranza-Edwards, A., Sanchez-Cabeza, J. A., & Ruíz-Fernández, A. C. (2015). Provenance and depositional history of continental slope sediments in the Southwestern Gulf of Mexico unraveled by geochemical analysis. *Continental Shelf Research*, 95, 15-26.

Auden, J. (1935). Traverses in the Himalaya. *Records of Geological survey of India*, 69, 123-167.

Audley-Charles, M. G. (1983). Reconstruction of eastern Gondwanaland. *Nature*, 306(5938), 48-50.

Augustsson, C., Aehnelt, M., Olivarius, M., Voigt, T., Gaupp, R., & Hilse, U. (2023). Provenance from the geochemical composition of terrestrial clastic deposits—A review with case study from the intracontinental Permo-Triassic of European Pangea. *Sedimentary Geology*, 456, 106496.

Baral, U., Ding, L., Dhital, M. R., Kumar, K. C., & Li, S. (2022). Paleozoic–Mesozoic dispersal of Gondwana: Insights from detrital zircon geochronology of Lesser Himalaya strata, eastern Nepal. *Bulletin*, *134*(9-10), 2345-2358.

Bashyal, R. P. (1980). Gondwana type of formation with phosphatic rocks in SE Nepal. *Journal Geological Society of India*, *21*(10), 484-491.

Bau, M. (1996). Controls on the fractionation of isovalent trace elements in magmatic and aqueous systems: evidence from Y/Ho, Zr/Hf, and lanthanide tetrad effect. *Contributions to Mineralogy and Petrology*, *123*(3), 323-333.

Bhandari, S., Xiao, W., Ao, S., Windley, B. F., Li, R., & Esmaeili, R. (2019). Detrital geochronology of the Gondwana sequence of the Lesser Himalaya of the Nepal Himalaya. *Geological Journal*, *54*(6), 3909-3920.

Canil, D. (1999). Vanadium partitioning between orthopyroxene, spinel and silicate melt and the redox states of mantle source regions for primary magmas. *Geochimica et Cosmochimica Acta*, *63*(3-4), 557-572.

Casshyap, S. M., & Kumar, A. (1987). Fluvial architecture of the Upper Permian Raniganj coal measure in the Damodar basin, Eastern India. *Sedimentary Geology*, *51*(3-4), 181-213.

Chakraborty, T., & Sarkar, S. (2005). Evidence of lacustrine sedimentation in the Upper Permian Bijori Formation, Satpura Gondwana basin: Palaeogeographic and tectonic implications. *Journal of Earth System Science*, *114*(3), 303-323.

Chowdari, S., Singh, B., & Singh, A. P. (2022). Anatomy of an intracratonic Son-Mahanadi Gondwana rift basin in Peninsular India: An integrated gravity, magnetic and remote sensing approach. *Physics of the Earth and Planetary Interiors*, *328*, 106888.

Cullers, R. L. (1994). The controls on the major and trace element variation of shales, siltstones, and sandstones of Pennsylvanian-Permian age from uplifted continental blocks in Colorado to platform sediment in Kansas, USA. *Geochimica et Cosmochimica Acta*, *58*(22), 4955-4972.

Dasgupta, S. (2021). A review of stratigraphy, depositional setting and Paleoclimate of the Mesozoic Basins of India. *Mesozoic Stratigraphy of India: A Multi-Proxy Approach*, 1-37.

Dasgupta, S., Banerjee, S., & Ghosh, P. (2022). Petrographical and geochemical study of syn-rift sediments, Pranhita-Godavari Intracratonic Gondwana Basin, India: genesis and paleo-environmental implications. *Geosciences*, *12*(6), 230.

DeCelles, P. G., Gehrels, G. E., Najman, Y., Martin, A. J., Carter, A., & Garzanti, E. (2004). Detrital geochronology and geochemistry of Cretaceous–Early Miocene strata of Nepal: implications for timing and diachroneity of initial Himalayan orogenesis. *Earth and Planetary Science Letters*, *227*(3-4), 313-330.

Dhital, M. R. (1992). Lithostratigraphic comparison of three diamictite successions of Nepal Lesser Himalaya. *Journal of Nepal Geological Society*, *8*, 43-54.https://doi.org/10.3126/jngs.v8i0.32601

Dhital, M. R. (2015). *Geology of the Nepal Himalaya: regional perspective of the classic collided orogen*. Springer. 498 p.

Dhital, M. R., & Kizaki, K. (1987). Lithology and Stratigraphy of the Northern Dang, Lesser Himaraya. *Bulletin of the College of Science, University of the Ryukyus/琉球大学理学部編*, (45), p183-243.

Dostal, J., & Capedri, S. (1978). Partition coefficients of gallium between minerals and silicate melts. *Contributions to Mineralogy and Petrology*, 67(2), 161-165.

Dutta, P. (2002). Gondwana lithostratigraphy of peninsular India. *Gondwana Research*, 5(2), 540-553.

Fedo, C. M., Wayne Nesbitt, H., & Young, G. M. (1995). Unraveling the effects of potassium metasomatism in sedimentary rocks and paleosols, with implications for paleoweathering conditions and provenance. *Geology*, *23*(10), 921-924.

Frank, W., & Fuchs, G. R. (1970). Geological investigations in west Nepal and their significance for the geology of the Himalayas. *Geologische Rundschau*, *59*(2), 552-580.

Gansser, A. (1964). Geology of the Himalayas Interscience Publishers London. *UK New York, NY, USA Sydney, Australia*, 289p.

Ghosh, S., & Sarkar, S. (2010). Geochemistry of Permo-Triassic mudstone of the Satpura Gondwana basin, central India: Clues for provenance. *Chemical Geology*, *277*(1-2), 78-100.

Gogoi, Y. K., Borgohain, P., Bhuyan, D., Bezbaruah, D., Konwar, G., Gogoi, M. P., & Bharali, B. (2025). Petrographic and geochemical perspectives on sandstones of the extra-peninsular Gondwana Group from the Arunachal Himalayas, NE India: Probing provenance, tectonic context and paleoenvironmental conditions. *Acta Geochimica*, 1-32.

Golonka, J., & Bocharova, N. Y. (2000). Hot spot activity and the break-up of Pangea. *Palaeogeography, Palaeoclimatology, Palaeoecology*, *161*(1-2), 49-69. https://doi.org/10.1016/S0031-0182(00)00117-6

Gupta, A. (1999). Early Permian palaeoenvironment in Damodar valley coalfields, India: an overview. *Gondwana Research*, *2*(2), 149-165.

Harnois, L. (1988). The CIW index: a new chemical index of weathering. *Sedimentary geology*, *55*(3), 319-322.

Hayashi, K. I., Fujisawa, H., Holland, H. D., & Ohmoto, H. (1997). Geochemistry of~ 1.9 Ga sedimentary rocks from northeastern Labrador, Canada. *Geochimica et cosmochimica acta*, 61(19), 4115-4137.

Herron, M. M. (1988). Geochemical classification of terrigenous sands and shales from core or log data. *Journal of Sedimentary Research*, 58(5), 820-829.

Hoskin, P. W. O., & Schaltegger, U. (2003). The composition of zircon and igneous and metamorphic petrogenesis. *Reviews in Mineralogy and Geochemistry*, 53(1), 27-62.

Kapoor, H. M., & Singh, G. (1987). Extra-peninsular Gondwana Basins-stratigraphy and evolution. *Journal of Palaeosciences*, *36*, 312-325. https://doi.org/10.54991/jop.1987.1590

Khadka, K., Sang, S., Han, S., He, J., Baral, U., Bhandari, S., & Mondal, D. (2025). Geochemical and Mineralogical Insights into Organic Matter Preservation in the Gondwana and Post-Gondwana Shale of the Lesser Himalayas, Nepal. *Minerals*, 15(1), 63.

Mackenzie, F. T., & Garrels, R. M. (1971). *Evolution of sedimentary rocks* (p. 397). New York: Norton.

Maejima, W., Das, R., Pandya, K. L., & Hayashi, M. (2004). Deglacial control on sedimentation and basin evolution of Permo-Carboniferous Talchir Formation, Talchir Gondwana Basin, Orissa, India. *Gondwana Research*, 7(2), 339-352.

Mall, D. M., & Sharma, S. R. (2009). Tectonics and thermal structure of western Satpura, India. *Journal of Asian Earth Sciences*, 34(3), 450-457.

McLennan, S. M. (1989). Rare earth elements in sedimentary rocks: influence of provenance and sedimentary processes. *Rev. Mineralogy Geochem*. 21, 169–200. doi:10.1515/9781501509032-010

McLennan, S. M., Bock, B., Hemming, S. R., Hurowitz, J. A., Lev, S. M., & McDaniel, D. K. (2003). The roles of provenance and sedimentary processes in the geochemistry of sedimentary rocks. *Geochemistry of sediments and sedimentary rocks: evolutionary considerations to mineral deposit-forming environments*, 4, 7-38.

McLennan, S. M., Hemming, S., McDaniel, D. K., & Hanson, G. N. (1993). Geochemical approaches to sedimentation, provenance, and tectonics. *In Processes controlling the composition of clastic sediments (pp. 21-40). Geological Society of America.*

Mishra, B., Pandya, K. L., & Maejima, W. (2004). Alluvial fan-lacustrine sedimentation and its tectonic implications in the Cretaceous Athgarh Gondwana Basin, Orissa, India. *Gondwana Research*, 7(2), 375-385.

Moradi, A. V., Sarı, A., & Akkaya, P. (2016). Geochemistry of the Miocene oil shale (Hançili Formation) in the Çankırı-Çorum Basin, Central Turkey: Implications for Paleoclimate conditions, source–area weathering, provenance and tectonic setting. *Sedimentary Geology*, 341, 289-303.

Nahak, S. K., Dasgupta, S., Prabhakar, N., & Banerjee, S. (2025). Correlation of Paleo-Mesozoic Sandstones Based on Heavy Mineral Chemistry and Th–U–Total Pb Monazite Dating: Implications on Paleogeographic Reconstruction in Eastern Gondwanaland. *Geological Journal*.

Najman, Y., Carter, A., Oliver, G., & Garzanti, E. (2005). Provenance of Eocene foreland basin sediments, Nepal: Constraints to the timing and diachroneity of early Himalayan orogenesis. *Geology*, *33*(4), 309-312.

Nesbitt, H. W., & Young, G. M. (1982). Early Proterozoic climates and plate motions inferred from major element chemistry of lutites. *nature*, 299(5885), 715-717.

Neupane, B., Ju, Y., Allen, C. M., Ulak, P. D., & Han, K. (2018). Petrography and provenance of Upper Cretaceous–Palaeogene sandstones in the foreland basin system of Central Nepal. *International Geology Review*, *60*(2), 135-156. 10.1080/00206814.2017.1312716

Pearce, J. A., Harris, N. B. W., & Tindle, A. G. (1984). Trace element discrimination diagrams for the tectonic interpretation of granitic rocks. *Journal of Petrology*, 25(4), 956-983.

Prıya, R. K., Tewari, V., & Ranjan, R. (2021). Geochemical and Petrological Studies of Permo-Carboniferous Sandstones from the Rangit Pebble-Slate Formation, Sikkim Lesser Himalaya, India: Implication for Provenance, Tectonic Setting, and Paleoclimate. *Türkiye Jeoloji Bülteni*, *64*(1), 129-142.

Rai, L. K., Acharya, K. K., & Dhital, M. R. (2016). Lithostratigraphy and structure of the Dharan–Mulghat area, Lesser Himalayan sequence, eastern Nepal Himalaya. *Journal of Nepal Geological Society*, *51*, 77-78. https://doi.org/10.3126/jngs.v51i0.24095

Rao, G. N. (1993). Geology and hydrocarbon prospects of East Coast sedimentary basins of India with special reference to Krishna Godavari basin. *Journal Geological Society of India*, 41(5), 444-454.

Robinson, D. M., & Pearson, O. N. (2013). Was Himalayan normal faulting triggered by initiation of the Ramgarh–Munsiari thrust and development of the Lesser Himalayan duplex?. *International Journal of Earth Sciences*, *102*(7), 1773-1790. https://doi.org/10.1007/s00531-013-0895-3

Rollinson, H. (1993). *Using Geochemical Data: Evaluation, Presentation, Interpretation*. Longman Scientific & Technical, Harlow.

Roser, B. P., & Korsch, R. J. (1986). Determination of tectonic setting of sandstone-mudstone suites using SiO2 content and K2O/Na2O ratio. *The Journal of Geology*, 94(5), 635-650.

Rudnick, R.L., and Gao, S., (2003). The composition of continental crust. In: Rudnick, R.L.(ed.), Treatise on geochemistry, vol.3, The Crust. Oxford:Elsevier, 1-64.

Saha, D., & Chaudhuri, A. K. (2003). Deformation of the Proterozoic successions in the Pranhita–Godavari basin, south India—a regional perspective. *Journal of Asian Earth Sciences*, 21(6), 557-565.

Sakai, H. (1983). Geology of the Tansen group of the Lesser Himalaya in Nepal. *Mem. Fac. Sci. Kyushu Univ, Ser. D, Geol.,* 15(1), 27-74. https://doi.org/10.5109/1546083

Schelling, D. (1992). The tectonostratigraphy and structure of the eastern Nepal Himalaya. *Tectonics*, *11*(5), 925-943.

Sharma, C. (1990). *Geology of Nepal Himalaya and adjacent countries*. Sangeeta Sharma, Bishal Nagar, Kathmandu Nepal, 479p.

Sharma, T., Kansakar, D. R., and Kizaki, K. (1984). Geology and tectonics of the region between Kali Gandaki and Bheri River in central west Nepal. *Bulletin of College of Science, University of the Ryukyus*, 38, 57-102.

Shrestha, S. B., Shrestha, J. N., and Sharma, S. R. (1987). *Geological map of mid-western Nepal (scale: 1250,000).* Department of Mines and Geology, Kathmandu.

Sitaula, R. (2009). *Petrofacies and paleotectonic evolution of Gondwanan and Post-Gondwanan sequences of Nepal* (Doctoral dissertation). Department of Geology and Geography Auburn University, 206p.

Sprague, R. A., Melvin, J. A., Conradi, F. G., Pearce, T. J., Dix, M. A., Hill, S. D., & Canham, H. (2009). Integration of core-based chemostratigraphy and petrography of the Devonian Jauf Sandstones, Uthmaniya area, Ghawar field, eastern Saudi Arabia. *Search and Discovery Article*, 20065, 34.

Storetvedt, K. M. (1990). The Tethys Sea and the Alpine-Himalayan orogenic belt; mega-elements in a new global tectonic system. *Physics of the Earth and Planetary Interiors*, *62*(1-2), 141-184. https://doi.org/10.1016/0031-9201(90)90198-7.

Sun, S. S., & McDonough, W. F. (1989). Chemical and isotopic systematics of oceanic basalts: implications for mantle composition and processes. *Geological Society, London, Special Publications*, *42*(1), 313-345.

Taylor, S. R., & McLennan, S. M. (1985). The continental crust: its composition and evolution.

Tewari, R. C., & Maejima, W. (2010). Origin of Gondwana basins of peninsular India. *Jour. Geosci*, *53*(3), 43-49.

Totten, M. W., Hanan, M. A., & Weaver, B. L. (2000). Beyond whole-rock geochemistry of shales: the importance of assessing mineralogic controls for revealing tectonic discriminants of multiple sediment sources for the Ouachita Mountain flysch deposits. *Geological Society of America Bulletin*, 112(7), 1012-1022.

Tripathi, C., & Singh, G. (1987). Gondwana and associated rocks of the Himalaya and their significance. *Gondwana Six: Stratigraphy, Sedimentology, and Paleontology*, *41*, 195-205. 10.1029/GM041p0195.

Ulak, P. D. (2016). *Geology of Nepal Himalaya*. Rachana Ulak, Kathmandu Nepal, 478 p.

Upreti, B. N. (1999). An overview of the stratigraphy and tectonics of the Nepal Himalaya. *Journal of Asian Earth Sciences*, *17*(5-6), 577-606.

Valdiya, K. S. (1995). Proterozoic sedimentation and Pan-African geodynamic development in the Himalaya. *Precambrian Research*, *74*(1-2), 35-55. https://doi.org/10.1016/0301-9268(95)00004-O

Valdiya, K. S. (1997). Himalaya, the northern frontier of East Gondwanaland. *Gondwana Research*, *1*(1), 3-9. https://doi.org/10.1016/S1342-937X(05)70002-2

Van der Voo, R., Spakman, W., & Bijwaard, H. (1999). Tethyan subducted slabs under India. *Earth and Planetary Science Letters*, *171*(1), 7-20. 10.1016/S0012-821X(99)00131-4.

Veevers, J. J. (2004). Gondwanaland from 650–500 Ma assembly through 320 Ma merger in Pangea to 185–100 Ma breakup: supercontinental tectonics via stratigraphy and radiometric dating. *Earth-Science Reviews*, *68*(1-2), 1-132. https://doi.org/10.1016/j.earscirev.2004.05.002.

Venkatachala, B. S., & Tiwari, R. S. (1987). Lower Gondwana marine incursions: periods and pathways. *Journal of Palaeosciences*, *36*, 24-29. https://doi.org/10.54991/jop.1987.1556

Wedepohl, K. H. (1995). The composition of the continental crust. *Geochimica et Cosmochimica Acta*, 59(7), 1217-1232.

Wei, W. E. I., & Algeo, T. J. (2020). Elemental proxies for paleosalinity analysis of ancient shales and mudrocks. *Geochimica et Cosmochimica Acta*, 287, 341-366.

Wilson, M. (1989). *Igneous Petrogenesis: A Global Tectonic Approach*. Unwin Hyman, London.

Wronkiewicz, D. J., & Condie, K. C. (1987). Geochemistry of Archean shales from the Witwatersrand Supergroup, South Africa: source-area weathering and provenance. *Geochimica et Cosmochimica Acta*, 51(9), 2401-2416.

Xiao, W., Zhang, B., Yang, K., Wang, Y., Wen, S., Ma, K., & Cao, G. (2023). Geochemical characteristics of the Upper Permian Longtan Formation from northeastern Sichuan Basin: Implications for the depositional environment and organic matter enrichment. *Acta Geologica Sinica-English Edition*, 97(4), 1196-1213.

Xie, G., Shen, Y., Liu, S., & Hao, W. (2018). Trace and rare earth element (REE) characteristics of mudstones from Eocene Pinghu Formation and Oligocene Huagang Formation in Xihu Sag, East China Sea Basin: Implications for provenance, depositional conditions and paleoclimate. *Marine and Petroleum Geology*, 92, 20-36.